

Lawrence Berkeley National Laboratory

LBL Publications

Title

BEYONDPLANCK

Permalink

<https://escholarship.org/uc/item/4z7669jm>

Authors

Gjerløw, E

Ihle, HT

Galeotta, S

et al.

Publication Date

2023-07-01

DOI

10.1051/0004-6361/202244061

Copyright Information

This work is made available under the terms of a Creative Commons Attribution License, available at <https://creativecommons.org/licenses/by/4.0/>

Peer reviewed

BEYONDPLANCK VII. Bayesian estimation of gain and absolute calibration for CMB experiments

E. Gjerløw^{1*}, H. T. Ihle¹, S. Galeotta², K. J. Andersen¹, R. Aurlien¹, R. Banerji¹, M. Bersanelli^{3,4,5}, S. Bertocco², M. Brilenkov¹, M. Carbone⁶, L. P. L. Colombo³, H. K. Eriksen¹, M. K. Foss¹, C. Franceschet^{3,5}, U. Fuskeland¹, M. Galloway¹, S. Gerakakis⁶, B. Hensley⁷, D. Herman¹, M. Iacobellis⁶, M. Ieronymaki⁶, J. B. Jewell⁸, A. Karakci¹, E. Keihänen^{9,10}, R. Keskitalo¹¹, G. Maggio², D. Maino^{3,4,5}, M. Maris², S. Paradiso^{3,5}, B. Partridge¹², M. Reinecke¹³, A.-S. Suur-Uski^{9,10}, T. L. Svalheim¹, D. Tavagnacco^{2,14}, H. Thommesen¹, D. J. Watts¹, I. K. Wehus¹, and A. Zacchei²

¹ Institute of Theoretical Astrophysics, University of Oslo, Blindern, Oslo, Norway

² INAF - Osservatorio Astronomico di Trieste, Via G.B. Tiepolo 11, Trieste, Italy

³ Dipartimento di Fisica, Università degli Studi di Milano, Via Celoria, 16, Milano, Italy

⁴ INAF-IASF Milano, Via E. Bassini 15, Milano, Italy

⁵ INFN, Sezione di Milano, Via Celoria 16, Milano, Italy

⁶ Planetek Hellas, Leoforos Kifisias 44, Marousi 151 25, Greece

⁷ Department of Astrophysical Sciences, Princeton University, Princeton, NJ 08544, U.S.A.

⁸ Jet Propulsion Laboratory, California Institute of Technology, 4800 Oak Grove Drive, Pasadena, California, U.S.A.

⁹ Department of Physics, Gustaf Hällströmin katu 2, University of Helsinki, Helsinki, Finland

¹⁰ Helsinki Institute of Physics, Gustaf Hällströmin katu 2, University of Helsinki, Helsinki, Finland

¹¹ Computational Cosmology Center, Lawrence Berkeley National Laboratory, Berkeley, California, U.S.A.

¹² Haverford College Astronomy Department, 370 Lancaster Avenue, Haverford, Pennsylvania, U.S.A.

¹³ Max-Planck-Institut für Astrophysik, Karl-Schwarzschild-Str. 1, 85741 Garching, Germany

¹⁴ Dipartimento di Fisica, Università degli Studi di Trieste, via A. Valerio 2, Trieste, Italy

May 23, 2022

ABSTRACT

We present a Bayesian calibration algorithm for CMB observations as implemented within the global end-to-end BEYONDPLANCK framework, and apply this to the *Planck* Low Frequency Instrument (LFI) data. Following the most recent *Planck* analysis, we decompose the full time-dependent gain into a sum of three nearly orthogonal components: One absolute calibration term, common to all detectors; one time-independent term that can vary between detectors; and one time-dependent component that is allowed to vary between one-hour pointing periods. Each term is then sampled conditionally on all other parameters in the global signal model through Gibbs sampling. The absolute calibration is sampled using only the orbital dipole as a reference source, while the two relative gain components are sampled using the full sky signal, including the orbital and Solar CMB dipoles, CMB fluctuations, and foreground contributions. We discuss various aspects of the data that influence gain estimation, including the dipole/polarization quadrupole degeneracy and processing masks. Comparing our solution to previous pipelines, we find good agreement in general, with relative deviations of -0.67% (-0.84%) for 30 GHz, 0.12% (-0.04%) for 44 GHz and -0.03% (-0.64%) for 70 GHz, compared to *Planck* DR4 (Planck 2018). We note that the BEYONDPLANCK calibration is performed globally, which results in better inter-frequency consistency than previous estimates. Additionally, *WMAP* observations are used actively in the BEYONDPLANCK analysis, and this both breaks internal degeneracies in the *Planck* data set and results in better overall agreement with *WMAP*. Finally, we use a Wiener filtering approach to smoothing the gain estimates. We show that this method avoids artifacts in the correlated noise maps due to over-smoothing the gain solution, which is difficult to avoid with methods like boxcar smoothing, as Wiener filtering by construction maintains a balance between data fidelity and prior knowledge. Although our presentation and algorithm are currently oriented toward LFI processing, the general procedure is fully generalizable to other experiments, as long as the Solar dipole signal is available to be used for calibration.

Key words. ISM: general – Cosmology: observations, polarization, cosmic microwave background, diffuse radiation – Galaxy: general

1. Introduction

The cosmic microwave background (CMB) anisotropies are among the most important observables available to cosmologists, and accurate determination of their statistical properties has been a main goal for a multitude of collaborations and experiments during the last three decades (e.g., Smoot et al. 1992; de Bernardis et al. 2000; Kovac et al. 2002; Bennett et al. 2013;

Planck Collaboration I 2020, and references therein). The BEYONDPLANCK project (BeyondPlanck 2022) is an initiative aiming to establish a common multi-experiment analysis platform that supports global end-to-end Bayesian analysis of raw time-ordered data (TOD) produced by such experiments, as well as seamless propagation of low-level uncertainties into all high-level products, including frequency and component maps, the CMB angular power spectra, and cosmological parameters. As a first demonstration, we apply this framework to the *Planck* LFI data, as presented in this and a suite of companion papers.

* Corresponding author: E. Gjerløw; eirik.gjerlow@astro.uio.no

A fundamentally important step in any CMB analysis pipeline is photometric calibration—the process of mapping the instrument readout to the incoming physical signal. In general, this procedure involves comparing some specific feature in the measured data with a known calibration model, for instance the CMB dipole or astrophysical foreground signal (or both), or by comparing the total measured power with a reference load with a known physical temperature (e.g., [Planck Collaboration V 2016](#)).

The multiplicative factor that converts between sky signal and detector readout is called the gain. This factor typically depends on the local environment of the detectors, such as the ambient temperature, and is therefore in principle different for each sample. However, as long as the detectors are thermally stable on reasonably long time scales, it is usually a good approximation to assume that the gain is constant over some short period of time, or at least that it is smoothly varying in time. For instance, the *WMAP* team adopted and fitted a six-parameter model for the gain, using housekeeping data such as focal plane temperature measurements to interpolate in time ([Jarosik et al. 2007](#); [Hinshaw et al. 2009](#); [Greason et al. 2012](#)). For LFI, we will assume that the gain factor is constant throughout each *Planck* pointing period (PID) – the timescale during which the satellite scans a given “circle” on the sky; these last roughly an hour each. We will also assume that the gain is varying smoothly between neighboring PIDs, except during a small set of events during which the instrument was actively modified by the mission control center, for instance during cooler maintenance.

The *Planck* LFI Data Processing Centre (DPC) ([Planck Collaboration II 2014](#); [Planck Collaboration V 2016](#); [Planck Collaboration II 2020](#)) used an onboard 4 K reference load to support the 30 GHz calibration for the early results, while for the other channels, and for all channels in later releases, they relied primarily on the CMB dipole signal. Gain fluctuations and correlations were modelled and suppressed by boxcar averaging over a signal-to-noise dependent window size. The *Planck* HFI DPC ([Planck Collaboration VIII 2014, 2016](#); [Planck Collaboration III 2020](#)) also used the CMB dipole signal for gain estimation, but in this case they assumed a constant gain factor throughout the whole mission, relying on the excellent thermal stability of the *Planck* instrument. Apparent gain variations were instead assumed to arise from non-linearities in the analog-to-digital conversion module, which then allowed for a deterministic correction. A similar approach has also been adopted by the recent SROLL2 re-analysis initiative ([Delouis et al. 2019](#)). We refer to the latest DPC maps as *Planck* 2018.

In the most recent official analysis (*Planck* DR4¹; [Planck Collaboration Int. LVII 2020](#)), the *Planck* team adopted the LFI gain model for all channels up to and including the 857 GHz channel. A novelty introduced in that analysis, however, was a decomposition of the gain factor into two nearly orthogonal components: an absolute (or baseline) gain factor, which was assumed to be constant for the entire mission, and a detector-specific gain mismatch factor that could vary both in time and between detectors. This approach allowed estimation of each component separately, using calibrators that are better suited to each component. For example, the low signal-to-noise (but well-understood) orbital dipole was used to calibrate the absolute gain factor due to the long integration time involved in estimating this particular component. Solving for all relevant factors was then performed jointly with other relevant quantities.

In this paper, we adopt the *Planck* DR4 approach, and decompose the full gain into the above-mentioned components, and we estimate these jointly with all other parameters in the full model. Thus, the main novel feature presented in this paper is the integration of the gain estimation procedure within a larger Gibbs framework, as summarized by [BeyondPlanck \(2022\)](#), which performs joint estimation of all relevant parameters in a statistically consistent manner, including the CMB and astrophysical foreground sky signal.

The rest of the paper is structured as follows: In Sect. 2, we aim to build intuition regarding gain estimation, presenting the general data model that we use and highlighting various important features of this model, as applied to real-world LFI observations. Next, in Sect. 3 we describe our main gain estimation procedure, before showing results in Sect. 5, and comparing these with those derived by other pipelines. Finally, we summarize in Sect. 6, with an eye toward future experiments and applications.

2. Data and modelling considerations

We start our presentation with a general discussion of the gain-related data model, and how to account for various complications that arise when fitting this to real-world data.

2.1. Data model

As described by [BeyondPlanck \(2022\)](#), the main goal of the BEYONDPLANCK analysis framework is to develop an end-to-end Bayesian analysis platform for CMB data, starting from raw time-ordered data. As for most Bayesian problems, the key step in our approach is therefore to write down an explicit parametric model for the observed data from a given detector, $d_{t,i}$, where t is the index denoting the sample,² and i is the index denoting the detector in question. In the current analysis, we adopt the following high-level model,

$$d_{t,i} = g_{t,i} s_{t,i}^{\text{tot}} + n_{t,i}^{\text{corr}} + n_{t,i}^{\text{wn}}, \quad (1)$$

where $n_{t,i}^{\text{corr}}$ and $n_{t,i}^{\text{wn}}$ are correlated and white noise, respectively, $g_{t,i}$ is the gain factor, and $s_{t,i}^{\text{tot}}$ denotes the total signal. Here, $s_{t,i}^{\text{tot}}$ is given in kelvin, while $d_{t,i}$ is the instrument readout, which is measured in volts, meaning that the unit for $g_{t,i}$ becomes [V/K]. The total signal can further be decomposed into

$$\begin{aligned} s_{t,i}^{\text{tot}} &= s_{t,i}^{\text{sky}} + s_{t,i}^{\text{orb}} + s_{t,i}^{\text{fsl}} \\ &= P_{tp,i} \mathbf{B}_{pp',i}^{\text{symm}} s_{p'}^{\text{sky}} + P_{tp,i} \mathbf{B}_{pp',i}^{\text{asymm}} s_{p'}^{\text{orb}} + P_{tp,i} \mathbf{B}_{pp',i}^{\text{asymm}} s_{p'}^{\text{fsl}} \\ &= P_{tp,i} \left[\mathbf{B}_{pp',i}^{\text{symm}} s_{p'}^{\text{sky}} + \mathbf{B}_{pp',i}^{\text{asymm}} \left(s_{p'}^{\text{orb}} + s_{p'}^{\text{fsl}} \right) \right]. \end{aligned} \quad (2)$$

In this expression, \mathbf{P} is the pointing matrix, which contains the mapping between the pointing direction the instrument, p and the sample index t ; \mathbf{B}^{symm} and $\mathbf{B}^{\text{asymm}}$ denote convolution with the symmetric and asymmetric beams, which quantify the fraction of the total signal coming from direction p' when the instrument is pointing towards p ; s^{sky} is the sky signal (including the Solar dipole); s^{orb} is the orbital dipole (to be discussed below); and s^{fsl} represents signal leakage through the far-sidelobes. For

² Here, a “sample” means the detector readout at every $1/f_{\text{samp}}$ seconds, where f_{samp} is the sampling frequency of the instrument. The whole set of these samples is called the time-ordered data (TOD). The sampling frequency for the three LFI instruments are 32.5 Hz, 46.5 Hz, and 78.8 Hz for the 30 GHz, 44 GHz, and 70 GHz instrument, respectively.

¹ Sometimes referred to as NPIPE.

further details regarding any of these objects, we refer the interested reader to [BeyondPlanck \(2022\)](#) and references therein.

The main topic of the current paper is estimating $g_{t,i}$. In this respect, it is important to note that all other free parameters in the data model, including $s_{t,i}^{\text{sky}}$ and $n_{t,i}^{\text{corr}}$, are also unknown, and must be estimated jointly with $g_{t,i}$. Casting this statement into Bayesian terms, we wish to sample from the *posterior distribution*,³

$$P(\mathbf{g}, \mathbf{s}^{\text{tot}}, \mathbf{s}^{\text{orb}}, \mathbf{n}^{\text{corr}}, \dots | \mathbf{d}). \quad (3)$$

That is, we aim to model the *global* state of the instrument and data, and map out the probability of various points in parameter space by sampling from this distribution. This may at first glance seem like a intractable problem. However, a central component of the BEYONDPLANCK framework is parameter estimation through *Gibbs sampling*. According to the theory of Gibbs sampling, samples from a joint posterior distribution may be drawn by iteratively sampling from all *conditional* distributions. In other words, when sampling the gain, we may assume that the sky signal and correlated noise parameters are perfectly known. And likewise, when sampling the sky signal or correlated noise parameters, we may assume that the gain is perfectly known. The correlations between these various parameters are then probed by performing hundreds or thousands of iterations of this type.

Thus, for the purposes of calibration alone, we do not need to be concerned with many aspects that indirectly affect the gain, such as CMB dipole or correlated noise estimation ([Planck Collaboration II 2014](#); [Planck Collaboration V 2016](#); [Planck Collaboration II 2020](#)). Instead, we are here concerned only with defining an adequate model for \mathbf{g} , and expressing this in a way that minimizes degeneracies with parameters in the Gibbs chain.

As discussed above, the gain is generally not constant in time. A very conservative (and somewhat naïve) model would therefore be to assume that the gain is in fact different for every sample t . However, this model clearly does not take into account our full knowledge about the instrument ([Planck Collaboration XXVIII 2014](#)). In particular, we do know that the gain is expected to correlate with the detector temperature, and this temperature does not change significantly on timescales of just one sample. Rather, based on available housekeeping data, a good assumption is that the gain is constant within a given pointing period (PID, or *scan*) – which is defined as a collection of samples measured over a period of about an hour, during which the instrument spins about its axis once per minute while keeping the spin axis vector stationary. Between each scan, the instrument performs a slight adjustment of the satellite spin axis, ensuring that new sky areas are covered in consecutive pointing periods.

To reflect the assumption of constant gain within each scan, we rewrite our data model as follows,

$$d_{t,i} = g_{q,i} s_{t,i}^{\text{tot}} + n_{t,i}^{\text{corr}} + n_{t,i}^{\text{wn}}, \quad (4)$$

where q now denotes PID. Thus, t is used to indicate a specific sample, while q represents a collection of samples.

From Eq. (4), we immediately note the presence of two important degeneracies, involving the sky signal and noise, respectively. If we attempt to fit for g , s^{tot} , and n^{corr} simultaneously, without knowing anything about any of them, we see that a given

solution, say, $\{g_0, s_0^{\text{tot}}, n_0^{\text{corr}}\}$, will result in an identical goodness-of-fit as another solution $\{g_1, s_1^{\text{tot}}, n_1^{\text{corr}}\}$, as long as either

$$g_1 = g_0 \frac{s_0^{\text{tot}}}{s_1^{\text{tot}}}, \quad (5)$$

or

$$n_1^{\text{corr}} = n_0^{\text{corr}} + g_0 s_0^{\text{tot}} - g_1 s_1^{\text{tot}}. \quad (6)$$

In other words, the gain is multiplicatively degenerate with the signal, and additively degenerate with the correlated noise. Such degeneracies are mainly a computational problem, since with two degenerate parameters in a Gibbs chain, exploring the resulting distributions takes a much larger number of samples than for uncorrelated parameters. A main topic of this paper is how to break these degeneracies in a statistically self-consistent and computationally efficient manner.

2.2. Absolute versus relative gain calibration

So far, we have been talking about the calibration of a given detector in isolation, which relates to what we call *absolute* calibration. Absolute calibration refers to correctly determining the “true” value of the gain, and is important for accurately determining the emitted intensity of astrophysical components, such as the CMB.

Another closely related concept is *relative* calibration,⁴ which quantifies calibration differences between radiometers. Because of *Planck*’s scanning strategy, which only provides weak cross-linking⁵ ([Planck Collaboration I 2011](#)), it is impossible to estimate the three relevant Stokes parameters (the intensity, I , and two linear polarization parameters, Q and U) independently for each detector. Rather, the polarization signal is effectively determined by considering pairwise differences between detector measurements, while properly accounting for their relative polarization angle differences at any given time. Therefore, any instrument characterization error that induces spurious detector differences will be partially interpreted by the analysis pipeline as a polarization signal. If our relative gain calibration is wrong, such differences will be introduced.

Given the high sensitivity of current and future CMB experiments, the gain must be estimated to a fractional precision better than $O(10^{-3})$ for robust CMB temperature analysis, and better than $O(10^{-4})$ for robust polarization analysis. Accurate relative calibration is thus even more important than accurate absolute calibration, and this will, as discussed in the next section, inform the choices we make on how to estimate these two types of calibration.

2.3. The Solar and orbital CMB dipoles

One of the most powerful ways to break the signal/gain degeneracy mentioned in the previous section is to observe a source of known brightness. If that source happens to be significantly

⁴ Note that our definition differs slightly from the *Planck* 2018 definition of relative calibration. In their nomenclature, relative calibration refers to temporal fluctuations of the gain around the mean within a given detector.

⁵ The scanning strategy adopted by *Planck* means that the time interval between successive measurements of the same point on the sky with the same detector from a different angle can be as much as six months (if the point lies along the ecliptic). During this time, several environmental parameters of the detector may have changed.

³ Here, and elsewhere, boldface quantities generally mean vectors. Which vector space they belong to will to a large degree be evident from the subscripts – in this case, there are no subscripts, meaning that the vectors contain all samples from all detectors.

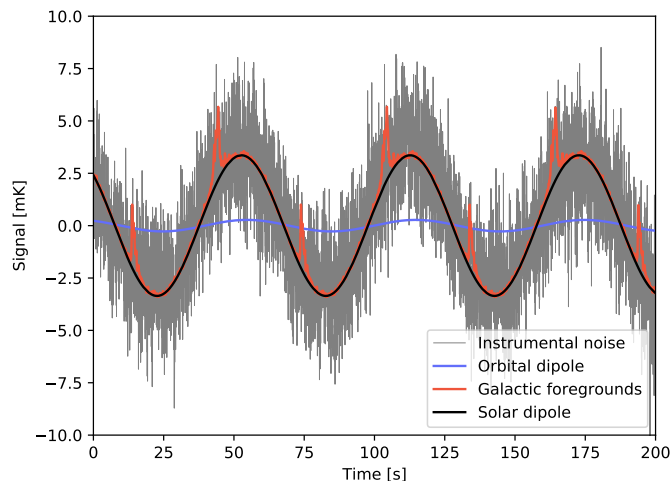


Fig. 1: Comparison of different contributions to the time-ordered data seen by *Planck* at 30 GHz, for a PID whose orientation is close to perpendicular to the dipole axis. The blue and black curves show the orbital and Solar CMB dipoles, respectively, while the red line shows contributions from small-scale CMB fluctuations and Galactic foregrounds. The gray line shows instrumental noise.

stronger than other sources in the same area of the sky, we could fix $s_{t,i}^{\text{tot}}$ in Eq. (4) and the gain would essentially be determined by the ratio of the data to the known source brightness.

Unfortunately, the number of available astrophysical calibration sources that may be useful for CMB calibration purposes is very limited, given the stringent requirements discussed in Sect. 2.2. For instance, the brightness temperature of individual planets within the Solar system is only known to about 5% (Planck Collaboration VIII 2016), while few other local sources are known with a precision better than 1%.

The key exception is the CMB dipole. The peculiar velocity of the *Planck* satellite relative to the CMB rest frame induces a strong apparent dipole on the sky due to the Doppler effect. Specifically, photons having an anti-parallel velocity relative to the satellite motion are effectively blue-shifted, while photons with a parallel velocity are redshifted.

It is useful to decompose the peculiar spacecraft velocity into two components; the motion of the Solar system relative to the CMB rest frame, $\mathbf{v}_{\text{solar}}$, and the orbital motion of the *Planck* satellite relative to the Solar system barycenter, $\mathbf{v}_{\text{orbital}}$. Thus, the total velocity of the satellite relative to the CMB rest frame is $\mathbf{v}_{\text{tot}} = \mathbf{v}_{\text{solar}} + \mathbf{v}_{\text{orbital}}$. Taking into account the full expression for the relativistic Doppler effect, the induced dipole reads

$$s^{\text{dip}}(\mathbf{x}, t) = T_{\text{CMB}} \left(\frac{1}{\gamma(t)(1 - \boldsymbol{\beta}(t) \cdot \mathbf{x})} - 1 \right), \quad (7)$$

where $\boldsymbol{\beta} = \mathbf{v}_{\text{tot}}/c$, and $\gamma = (1 - |\boldsymbol{\beta}|^2)^{-1/2}$. The total dipole is time dependent because of the motion of the satellite over the course of the mission. We can similarly define a Solar dipole, $s^{\text{solar}}(\mathbf{x})$ and an orbital dipole, $s^{\text{orb}}(\mathbf{x}, t)$, which are induced by only the Solar and orbital velocities alone, respectively. Both dipoles play crucial roles in CMB calibration; the orbital dipole for absolute calibration and the Solar dipole for relative calibration.

Starting with the orbital dipole, we note that this depends only on the satellite's velocity with respect to the Sun. This is exceedingly well measured through radar observations, and known with a precision better than 1 cm s^{-1} (Godard et al. 2009). For

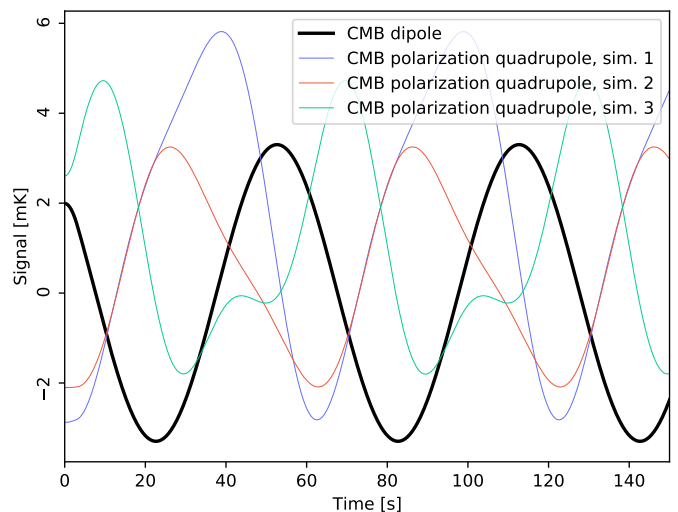


Fig. 2: Comparison of the CMB temperature dipole (thick black line) observed through the *Planck* scanning strategy with three random polarization quadrupole simulations (thin colored lines); the latter have been scaled by a factor of 10^4 for visualization purposes.

an orbital speed of 30 km s^{-1} , this results in an overall relative precision better than $O(10^{-6})$. However, Eq. (7) also depends on the CMB monopole, which is measured by *COBE-FIRAS* to $2.72548 \text{ K} \pm 0.57 \text{ mK}$ (Fixsen 2009), corresponding to a relative uncertainty of 0.02% or $O(10^{-4})$. Thus, the absolute calibration of any current and future CMB experiment cannot be determined with a higher absolute precision than $O(10^{-4})$ until a next-generation CMB spectral distortion experiment, for instance PIXIE (Kogut et al. 2011), is launched. Still, this precision is more than sufficient for *Planck* calibration purposes.

The second CMB dipole component corresponds to the Sun's motion with respect to the CMB rest frame. While this velocity is intrinsically unknown, one may estimate this from the relative amplitude of the Solar and orbital dipoles. This is illustrated in Fig. 1, which compares the orbital and Solar dipole signals (blue and black curves) with contributions from Galactic foreground emission and instrumental noise at 30 GHz for about three minutes of time-ordered observations. The Solar dipole is effectively determined by the relative amplitude ratio between the black and blue curves in this figure.

Based on this approach, the most recent *Planck* analyses have determined that the Solar CMB dipole amplitude is about 3.36 mK , corresponding to Solar velocity of about 370 km s^{-1} (Planck Collaboration I 2020; Planck Collaboration Int. LVII 2020). For comparison, large-scale CMB polarization fluctuations typically exhibit variations smaller than $O(1 \mu\text{K})$ (Planck Collaboration IV 2018), and consequently the relative calibration of different detectors must be better than $O(10^{-4})$ to avoid significant contamination of the polarization signal by the Solar CMB dipole. Achieving this level of precision in the presence of correlated noise, Galactic foregrounds, far sidelobe contamination and other sources of systematic uncertainties is the single most difficult challenge associated with large-scale CMB polarization science.

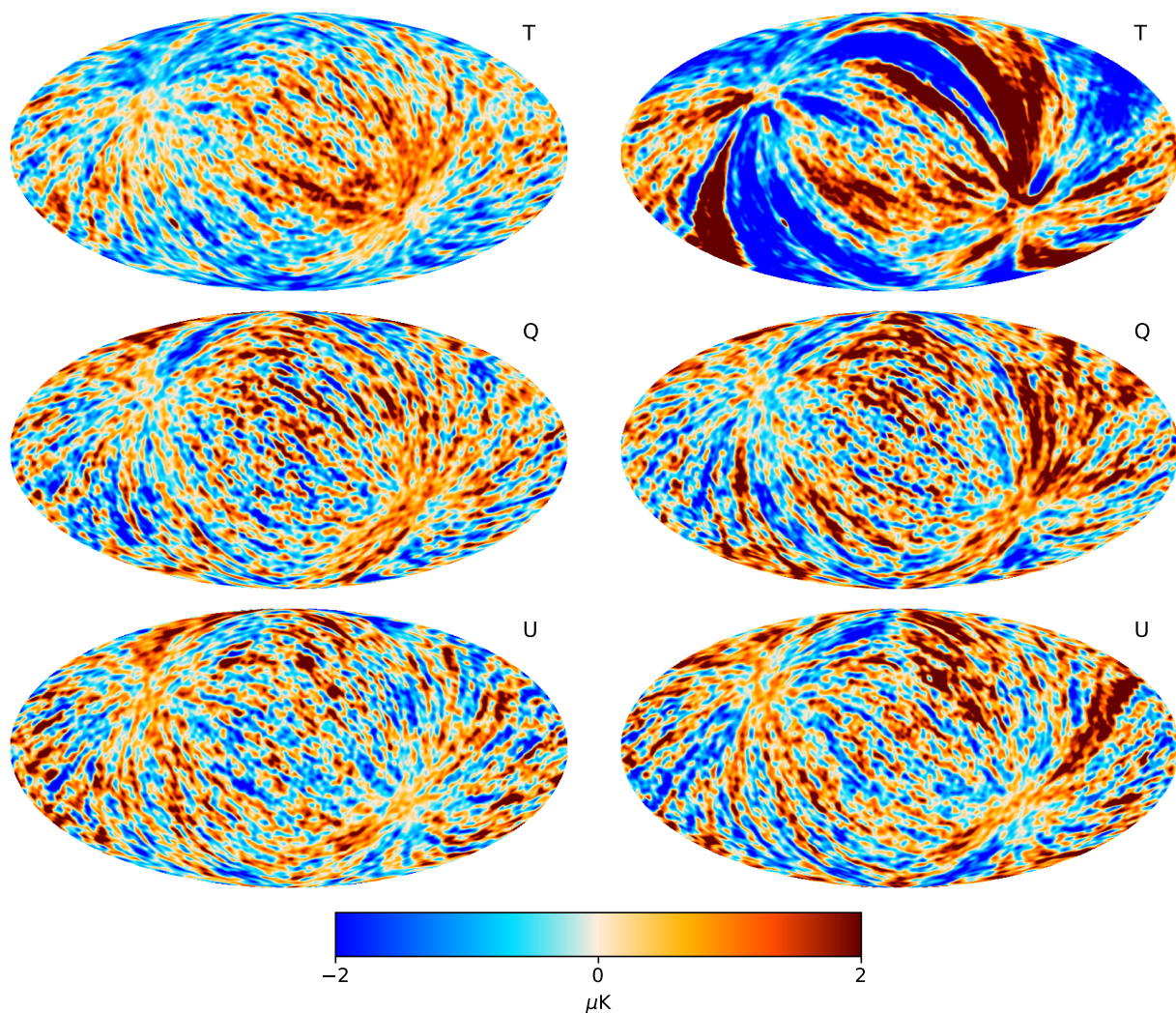


Fig. 3: Correlated noise maps for the 30 GHz channel in a Gibbs chain that includes (*left panel*) or neglects (*right panel*) gain time-dependencies. All maps are smoothed to a common resolution of 2.5° FWHM.

2.4. The degeneracy between the CMB temperature dipole and polarization quadrupole

In Sect. 2.1 we noted that the gain is multiplicatively degenerate with the signal, and additively degenerate with the noise. Within this broad categorization, there are also some particularly important gain/signal degeneracies that are worth highlighting, and perhaps the most prominent example is that with respect to the CMB polarization quadrupole. To illustrate this, consider the case in which two detectors report different CMB dipole amplitude signals; how could such a difference be explained? One possible explanation is a calibration mismatch, i.e., that the absolute calibration of one or both detectors is mis-estimated.

Another possible explanation could be a large polarization CMB *quadrupole* signal. Due to the scanning strategy adopted by *Planck*, in which the same ring is observed repeatedly for one hour, a polarization quadrupole can easily appear with a dipolar signature, depending on the particular phase orientation of the mode in question. This is illustrated in Fig. 2. The black thick line shows the CMB temperature dipole as a function of time, while the colored thin lines show three random polarization quadrupole simulations, all observed with the *Planck* scanning strategy. Out of the three random quadrupole simulations,

two have a time-domain behaviour that very closely mimics the CMB temperature dipole, and in the presence of noise and instrumental effects, it would be exceedingly difficult to distinguish between the two models.

This is a perfect recipe for a degenerate system, and one that carries the potential of contaminating any large-scale polarization reconstruction. It is, however, important to note that this particular degeneracy appears with a very specific morphology, and affects only a handful of spatial polarization modes, as defined by projecting the CMB Solar dipole onto the *Planck* scanning strategy. Recognizing the importance of this degeneracy, previous *Planck* analyses have adopted different strategies of resolving the issue. For instance, both the *Planck* 2018 and *Planck* DR4 analyses have opted to disregard the CMB polarization component completely during the calibration phase (*Planck Collaboration II* 2016, 2020; *Planck Collaboration Int. LVII* 2020). This may be at least partially justified for LFI on theoretical grounds by noting that the CMB polarization variance on large angular scales predicted by current best-fit Λ CDM models is $\lesssim 0.1 \mu\text{K}^2$, which is comparable to, or below, the overall noise. For the significantly more sensitive HFI instrument, this assumption is not adequate, and the recent *Planck* DR4 analysis

therefore explicitly estimates a transfer function to account for this effect (Planck Collaboration Int. LVII 2020).

In the following, we adopt a slightly different strategy: We include the CMB polarization component in the calibration procedure, using the current sample in the Gibbs chain. In order to break the abovementioned degeneracy, we replace the polarization quadrupole of the CMB map with a random value drawn from the best-fit Λ CDM model, using a value of $D_2^{EE} = 0.0308827 \mu\text{K}^2$. Thus, we marginalize over this component and propagate the uncertainties introduced by this naturally into the Gibbs samples. We expect the combined effect of this addition to be negligible, because of the low value of the Λ CDM prediction, and as shown in Brilenkov et al. (2022) the gain estimation is unaffected by this marginalization.

2.5. Processing masks and PID selection

The Gibbs sampling framework used by BEYONDPLANCK requires an explicit parametric model that describes CMB, foregrounds, and the instrument. If this model turns out to be an insufficient representation of the actual data, the Gibbs sampling framework will attempt to fit eventual modelling errors using the parameters that are at its disposal. Ideally, such unexplained contributions should end up as an excess residual in $\mathbf{r} = \mathbf{d} - \mathbf{g}\mathbf{s}^{\text{tot}} - \mathbf{n}^{\text{tot}}$, but in practice they often also contaminate the other model parameters, such as the CMB. The correlated noise, \mathbf{n}^{corr} , is one such parameter that, because of its relatively unconstrained and global structure, ends up absorbing a wide range of modelling errors, as discussed by Ihle et al. (2022). Furthermore, as already noted in Sect. 2.1, there is a tight degeneracy between the correlated noise and the gain, and \mathbf{n}^{corr} is therefore a sensitive monitor for gain errors. Figure 3 illustrates this in terms of one arbitrarily selected 30 GHz \mathbf{n}^{corr} sample from the main BEYONDPLANCK analysis (BeyondPlanck 2022). The left column shows such a sample in the default model, in which the gain is allowed to vary from PID to PID, while the right column shows the same when enforcing a time-independent gain. While the maps in the left column are visually dominated by scan-aligned random stripes, as expected for \mathbf{n}^{corr} , the maps in the right column (in particular the top row) show large excesses with a dipolar pattern along each *Planck* scanning ring. This is the archetypal signature of gain modelling errors, and this clearly demonstrates the need for a time-variable gain model. At the same time, there is also a clear quadrupolar pattern in the default configuration, with a positive excess along the Galactic plane and a negative excess near the Galactic poles. This structure is visually consistent with a near sidelobe modelling residual, in the sense that the Galactic foreground signal is slightly over-smoothed compared to the prediction of the nominal beam model, and the resulting residual is picked up by the correlated noise component. This is not surprising, considering that about 1% of the full LFI 30 GHz beam solid angle is unaccounted for in the GRASP beam model (Planck Collaboration II 2020), and some of this missing power may be in the near sidelobes. Fortunately, we also see from the same plot that the impact of this effect is modest, and accounts for only about $1 \mu\text{K}$ at 30 GHz.

More generally, because we have an incomplete understanding of both the instrument and the microwave sky, modelling errors will at some level always be a concern when estimating both gain and correlated noise. Furthermore, these modelling errors will typically be stronger near the Galactic plane or bright compact sources, where foreground uncertainties are large. For this reason, it is customary to apply a processing mask while es-

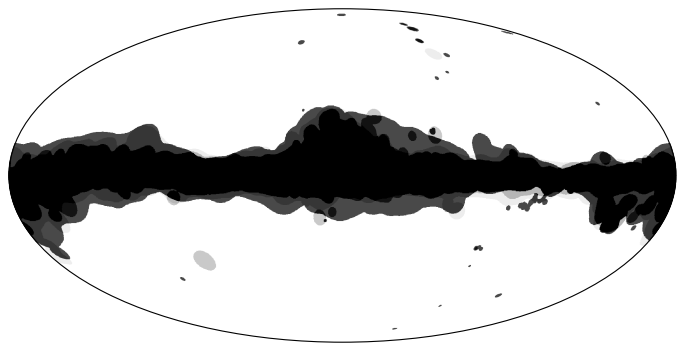


Fig. 4: Processing masks used in gain and correlated noise estimation. Different shades of grey indicate different frequency masks. The allowed 30 GHz sky fraction (light) is 0.73, the 44 GHz sky fraction (intermediate) is 0.81, and the 70 GHz sky fraction (dark) is 0.77. Reproduced from Ihle et al. (2022).

timating these quantities, omitting the parts of the sky that are least understood from the analysis. In BEYONDPLANCK, we define processing masks based on data-minus-signal residual maps for each frequency (Ihle et al. 2022), which are shown in Fig. 4.

In addition, as discussed by Suur-Uski et al. (2022), we also exclude a number of PIDs from the main analysis, for similar reasons as for applying processing masks. Most of these PIDs, however, do not correspond to particularly problematic areas of the sky, but rather to unmodelled instrumental changes or systematic errors, such as cooler maintenance or major satellite maneuvers. Excluded PIDs will show up as gaps in all PID plots in this paper.

2.6. Breaking degeneracies through multi-experiment analysis

As described in BeyondPlanck (2022), BEYONDPLANCK includes as part of its data selection several external data sets that are necessary to break fundamental degeneracies within the model. One particularly important example in this respect is the inclusion of low-resolution *WMAP* polarization data. In the same way that the *WMAP* experiment was unable to measure a few specific polarization modes on the sky due to peculiarities in its scanning strategy (Jarosik et al. 2007), *Planck* is also unable to constrain some modes as defined by its scanning strategy (Planck Collaboration II 2020). However, because the *WMAP* and *Planck* scanning strategies are intrinsically very different, their degenerate modes are not the same, and, therefore all sky modes may be measured to high precision when analyzing both data sets jointly.

This will be explicitly demonstrated in Sect. 5.4, where we compare the BEYONDPLANCK sky maps to those derived individually from each experiment. The morphology of these frequency difference maps correspond very closely to the correction templates produced respectively by the *WMAP* and *Planck* teams (Jarosik et al. 2007; Planck Collaboration II 2020), and BEYONDPLANCK is statistically consistent with both data sets. Agreement is a direct and natural consequence of performing a joint fit, and there is no need for additional explicit template corrections for BEYONDPLANCK.

At the same time, it is also important to note that only the *Planck* LFI data are currently modelled in terms of time-ordered data, whereas the *WMAP* sky maps and noise covariance matrices are analyzed as provided by the *WMAP* team. Therefore, if there should be unknown systematics present in *WMAP*, those

errors will necessarily also propagate into the various BEYOND-PLANCK products. An important near-future goal is therefore to integrate also the *WMAP* time-ordered data into this framework. This work is already on-going, as discussed by Watts et al. (2022), but a full *WMAP* TOD-based analysis lies beyond the scope of the current work.

3. Methodology

As discussed in Sect. 2.1, our main goal in this paper is to draw samples from $P(\mathbf{g} | s^{\text{tot}}, \mathbf{n}^{\text{corr}}, \mathbf{d}, \dots)$, the conditional distribution of \mathbf{g} given all other parameters. In this section, we describe each of the various steps involved in this process.

3.1. Correlated noise degeneracies and computational speed-up

Before we present our main sampling algorithms for \mathbf{g} , we recall from Sect. 2.1 that \mathbf{g} is additively degenerate with \mathbf{n}^{corr} . In a Gibbs sampling context, strong degeneracies lead to very long Markov correlation lengths as the Gibbs sampler attempts to explore the degenerate space between the two parameters. In order to save computing power and time, it is therefore better to sample \mathbf{g} and \mathbf{n}^{corr} jointly, such that for a given iteration of the main Gibbs chain, we instead sample directly from $P(\mathbf{g}, \mathbf{n}^{\text{corr}} | s^{\text{tot}}, \mathbf{d}, \dots)$.⁶

A joint sample may be produced by means of univariate distributions through the definition of a conditional distribution,

$$P(x_1 | x_2) \equiv \frac{P(x_1, x_2)}{P(x_2)} \Rightarrow P(x_1, x_2) = P(x_1 | x_2)P(x_2). \quad (8)$$

Thus, sampling from the joint distribution $P(\mathbf{g}, \mathbf{n}^{\text{corr}} | s^{\text{tot}}, \mathbf{d}, \dots)$ is equivalent to first sampling \mathbf{g} from its *marginal* distribution with respect to \mathbf{n}^{corr} , $P(\mathbf{g} | s^{\text{tot}}, \mathbf{d}, \dots)$, and then subsequently sampling \mathbf{n}^{corr} from its *conditional* distribution with respect to \mathbf{g} , $P(\mathbf{n}^{\text{corr}} | \mathbf{g}, s^{\text{tot}}, \mathbf{d}, \dots)$. These two steps must be performed immediately after one another, or else we would introduce an inconsistency in the Gibbs chain with respect to the other parameters.

Note that $P(\mathbf{n}^{\text{corr}} | \mathbf{g}, s^{\text{tot}}, \mathbf{d}, \dots)$ is unchanged compared to the original Gibbs prescription, and no changes are required to sample from that particular distribution (see Ihle et al. 2022, for more details on this sampling process). When it comes to $P(\mathbf{g} | s^{\text{tot}}, \mathbf{d}, \dots)$, we refer to Appendix A.2 of BeyondPlanck (2022), whose sampling equations we will use throughout this paper. We note that the data model used in that appendix is the same general form as Eq. (4), and that sampling from $P(\mathbf{g} | s^{\text{tot}}, \mathbf{d}, \dots)$ is exactly analogous to what is shown in that appendix, as long as we make the identification $\mathbf{n} \rightarrow \mathbf{n}^{\text{corr}} + \mathbf{n}^{\text{wn}}$. As the covariance matrix of a sum of independent Gaussian variables (\mathbf{n}^{corr} and \mathbf{n}^{wn}) is also Gaussian, with a covariance matrix given by the sum of the individual covariance matrices, we can in what follows use the results of the above-mentioned appendix to sample from $P(\mathbf{g} | s^{\text{tot}}, \mathbf{d}, \dots)$ as long as we let $\mathbf{N} \rightarrow \mathbf{N}^{\text{corr}} + \mathbf{N}^{\text{wn}}$.

Computationally speaking, sampling from $P(\mathbf{g} | s^{\text{tot}}, \mathbf{d}, \dots)$ instead of $P(\mathbf{g} | s^{\text{tot}}, \mathbf{n}^{\text{corr}}, \mathbf{d}, \dots)$ is numerically equivalent to a more expensive noise covariance matrix evaluation.⁷ To mitigate this additional cost, we note that the gain is assumed to be slowly

⁶ Although this might seem somewhat counter-intuitive in the context of Gibbs sampling, joint sampling formally corresponds to reparametrizing $\{\mathbf{g}, \mathbf{n}^{\text{corr}}\}$ into *one* parameter in the Gibbs chain.

⁷ Although not shown here, sampling from $P(\mathbf{g} | s^{\text{tot}}, \mathbf{n}^{\text{corr}}, \mathbf{d}, \dots)$ would follow the exact same procedure, but with a noise covariance ma-

trix given by \mathbf{N}^{wn} instead of $\mathbf{N}^{\text{wn}} + \mathbf{N}^{\text{corr}}$. \mathbf{N}^{wn} is a diagonal matrix, while \mathbf{N}^{corr} is not, and since most operations are less heavy, computationally speaking, when diagonal matrices are involved, the resulting sampling process would also be lighter in that case.

3.2. Absolute gain calibration with the orbital dipole

Next, we also recall from Sect. 2.1 that the gain is multiplicatively degenerate with the total sky signal. At the same time, we note that the orbital CMB dipole is known to exquisite precision, and this particular component is therefore the ideal calibrator for CMB satellite experiments. However, its relatively low amplitude as compared with instrumental noise renders it incapable of tracking short-term gain variations, and, when fitted jointly with astrophysical foregrounds, it is also not sufficiently strong to determine relative calibration differences between detectors at the precision required for large-scale polarization reconstruction. Therefore, to minimize sensitivity to potential residual systematic and modelling errors, it is advantageous to estimate the absolute calibration using the orbital dipole alone, but use the full signal model (including the bright Solar CMB dipole) when estimating relative and time-dependent gain variations.

This motivates splitting the gain into two components,

$$g_{q,i} = g_0 + \gamma_{q,i}, \quad (9)$$

where g_0 is now independent of both time and detectors, following Planck Collaboration Int. LVII (2020). Our goal is then to use only the orbital CMB dipole to estimate g_0 , and later use the full sky signal to estimate $\gamma_{q,i}$. Thus, with this reparametrization, we go from sampling from $P(\mathbf{g} | s^{\text{tot}}, \mathbf{d}, \dots)$ to sampling from $P(g_0, \boldsymbol{\gamma} | s^{\text{tot}}, \mathbf{d}, \dots)$. As usual, drawing samples from this joint distribution can be done by Gibbs sampling, so that we first sample g_0 from $P(g_0 | \boldsymbol{\gamma}, s^{\text{tot}}, \mathbf{d}, \dots)$ and then $\boldsymbol{\gamma}$ from $P(\boldsymbol{\gamma} | g_0, s^{\text{tot}}, \mathbf{d}, \dots)$.

We should note that estimating g_0 using only the orbital dipole formally represents a violation of the Gibbs formalism, as we no longer draw this particular parameter from its exact conditional distribution. This is one of many examples for which we “buy” stability with respect to systematic errors at the price of increased statistical uncertainties. This is similar to the application of a processing mask when estimating the zero-levels of a CMB sky map (e.g., Planck Collaboration Int. XLVI 2016), or fitting correlated noise parameters using only a sub-range of all available temporal frequencies (e.g., Ihle et al. 2022). In all such cases, parts of the data are disregarded in order to prevent potential systematic errors from contaminating the parameter in question.

For the split in Eq. (9) to be valid, we must ensure that $\sum_{q,i} \gamma_{q,i} = 0$, such that $\gamma_{q,i}$ represents only deviations from the absolute calibration. For technical reasons, it turns out that this will be easier to do if we also reparametrize $\gamma_{q,i}$,

$$\gamma_{q,i} = \Delta g_i + \delta g_{q,i}, \quad (10)$$

where Δg_i represents the detector-specific constant gain, and $\delta g_{q,i}$ denotes deviations from Δg_i per scan. We can then separately enforce $\sum_i \Delta g_i = 0$ and $\sum_q \delta g_{q,i} = 0$ for each detector

trix given by \mathbf{N}^{wn} instead of $\mathbf{N}^{\text{wn}} + \mathbf{N}^{\text{corr}}$. \mathbf{N}^{wn} is a diagonal matrix, while \mathbf{N}^{corr} is not, and since most operations are less heavy, computationally speaking, when diagonal matrices are involved, the resulting sampling process would also be lighter in that case.

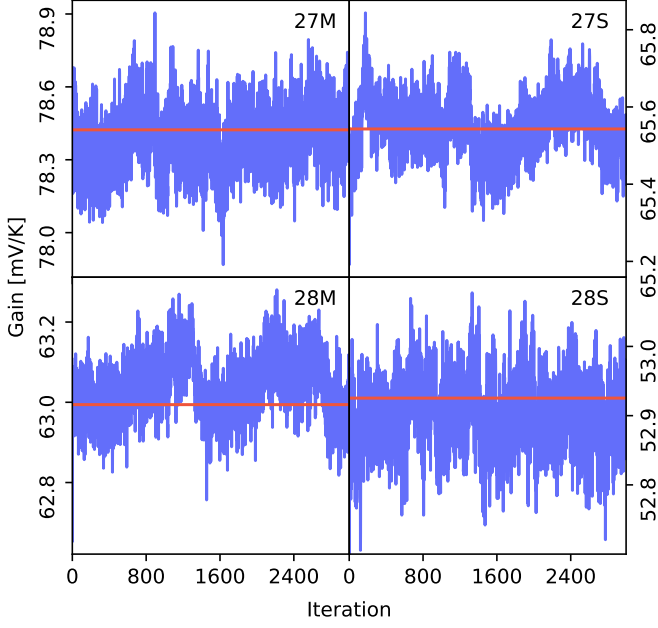


Fig. 5: Trace plots of samples of the total gain for randomly selected PIDs for each of the four 30 GHz detectors for our simulation run. The PIDs are, respectively, 349, 9847, 4298, and 1993. The red lines signify the input gain values.

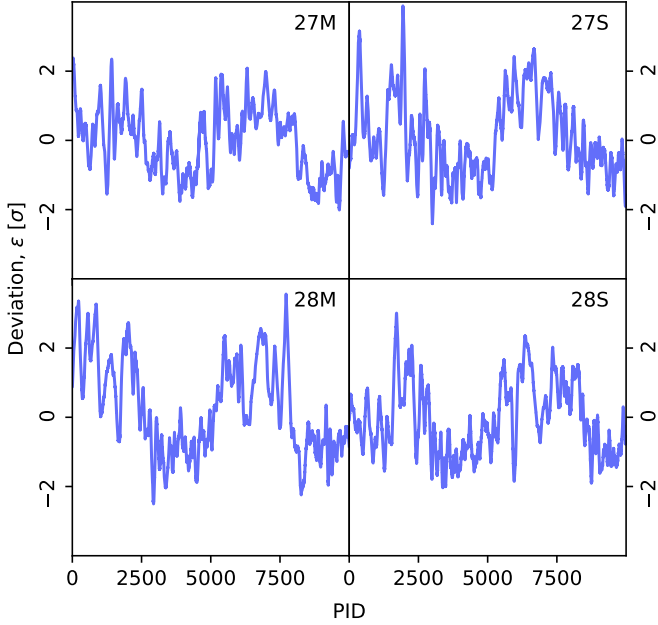


Fig. 6: Deviation of the mean output gain solution from the input gain for each PID and 30 GHz detector in our simulation run. The deviations are measured in sample standard deviations.

i , which is computationally cheaper than enforcing both constraints simultaneously.

Thus, we split the gain into three nearly independent variables, and explore their joint distribution by Gibbs sampling. The overarching goal for this section, then, is to derive sampling algorithms for each of the three associated conditional distribu-

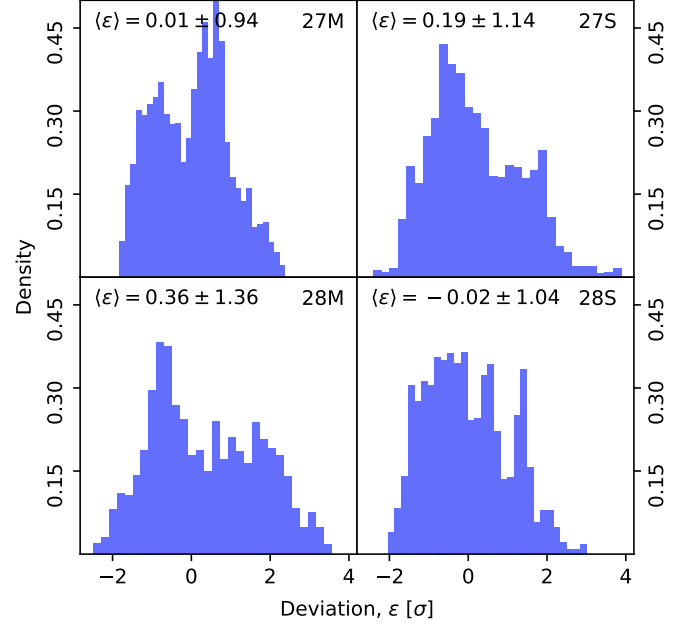


Fig. 7: Histograms of the deviations of the mean output gain solution from the input gain, given in number of sample standard deviations in our simulation run. Each histogram represents the aggregation of the 10,000 PIDs included in the simulation validation.

tions,

$$P(g_0 | \Delta g_i, \delta g_{q,i}, \mathbf{d}_i, \mathbf{s}_i^{\text{tot}}, N_i, \dots) \quad (11)$$

$$P(\Delta g_i | g_0, \delta g_{q,i}, \mathbf{d}_i, \mathbf{s}_i^{\text{tot}}, N_i, \dots) \quad (12)$$

$$P(\delta g_{q,i} | g_0, \Delta g_i, \mathbf{d}_i, \mathbf{s}_i^{\text{tot}}, N_i, \dots). \quad (13)$$

We now consider each of these in turn.

3.3. Sampling the absolute calibration, g_0

To sample the absolute calibration using the orbital dipole alone, we need to define a data model that depends only on g_0 and s^{orb} . We do this by first subtracting the full signal model as defined by the current joint parameter state, and then add back only the orbital dipole term,

$$\begin{aligned} r_{t,i} &\equiv d_{t,i} - (g_0^{\text{curr}} + \Delta g_i + \delta g_{q,i}) s_{t,i}^{\text{tot}} + g_0^{\text{curr}} s_{t,i}^{\text{orb}} \\ &= g_0 s_{t,i}^{\text{orb}} + n_{t,i}^{\text{tot}}. \end{aligned} \quad (14)$$

Here g_0^{curr} denotes the absolute gain at the *current* iteration in the Gibbs chain, i.e., before drawing a new value for g_0 .

As noted earlier, working with this residual and using the previous sample of g_0 to estimate the current sample does represent a breaking of the Gibbs formalism, since the statistically exact residual for g_0 would be

$$d_{t,i} - (\Delta g_i + \delta g_{q,i}) s_{t,i}^{\text{tot}} = g_0 s_{t,i}^{\text{tot}} + n_{t,i}^{\text{tot}}. \quad (15)$$

However, in this case we would also be calibrating g_0 on the total sky signal instead of just the orbital dipole. Thus, we trade mathematical rigour and statistical uncertainties for stronger robustness with respect to systematic effects.

As discussed in Sect. 3.1, the noise term in Eq. (14) includes both correlated and white noise, and the appropriate covariance

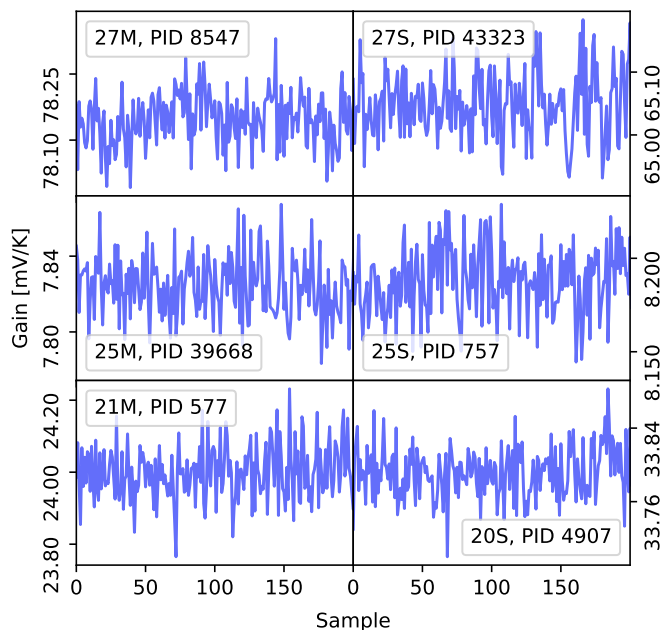


Fig. 8: Gibbs chains of the total gain for selected detectors and PIDs.

matrix is therefore $\mathbf{N} = \mathbf{N}^{\text{corr}} + \mathbf{N}^{\text{wn}}$. Given this fact, Eq. (14) corresponds to a simple uni-variate Gaussian model as a function of g_0 , and the appropriate sampling algorithm is discussed in Appendix A.2 of [BeyondPlanck \(2022\)](#). Applying that general procedure to our special case, we may write down the following sampling equation for \hat{g}_0 ,⁸

$$\hat{g}_0 = \frac{\sum_i (s_i^{\text{orb}})^T \mathbf{N}_i^{-1} \mathbf{r}_i}{\sum_i (s_i^{\text{orb}})^T \mathbf{N}_i^{-1} s_i^{\text{orb}}} + \frac{\eta}{\sqrt{\sum_i (s_i^{\text{orb}})^T \mathbf{N}_i^{-1} s_i^{\text{orb}}}}, \quad (16)$$

where $\eta \sim N(0, 1)$ is a random number drawn from a standard normal distribution. Here, and elsewhere, a T superscript indicates the matrix transpose operator. The first term in this equation is the (Wiener filter) mean of the distribution $P(g_0 | \mathbf{r}_i, \mathbf{N}_i)$, while the second term ensures that g_0 has the correct variance.

3.4. Sampling detector-dependent calibration

For Δg_i , we proceed similarly as with g_0 , with two exceptions. First, Δg_i now represents the relative calibration between detectors, and, as discussed in Sect. 2.1, we need to use a stronger calibration signal than the orbital dipole to avoid significant polarization leakage. Secondly, we have to impose the constraint $\sum_i \Delta g_i = 0$.

We start by defining the following residual,

$$r_{i,i} \equiv d_{i,i} - (g_0 + \delta g_{q,i}) s_i^{\text{tot}} = \Delta g_i s_i^{\text{tot}} + n_i^{\text{tot}} \quad (17)$$

for each detector. This equation is structurally similar to Eq. (14), with the main difference being that the total sky signal, which is

⁸ Note that we do not apply any priors on g_0 in this paper, which corresponds to $\mathbf{S}^{-1} = 0$, adopting the notation of [BeyondPlanck \(2022\)](#), where \mathbf{S} is the prior covariance of g_0 . The remaining notational differences between Eq. (16) and Eq. (A.10) in that paper arise from our organizing all vectors and matrices in terms of independent detectors, using the fact that \mathbf{n}^{tot} is assumed to be independent between detectors; this may not be strictly true in practice, as discussed by [Ihle et al. \(2022\)](#), and future analyses may prefer to account for the full joint matrix.

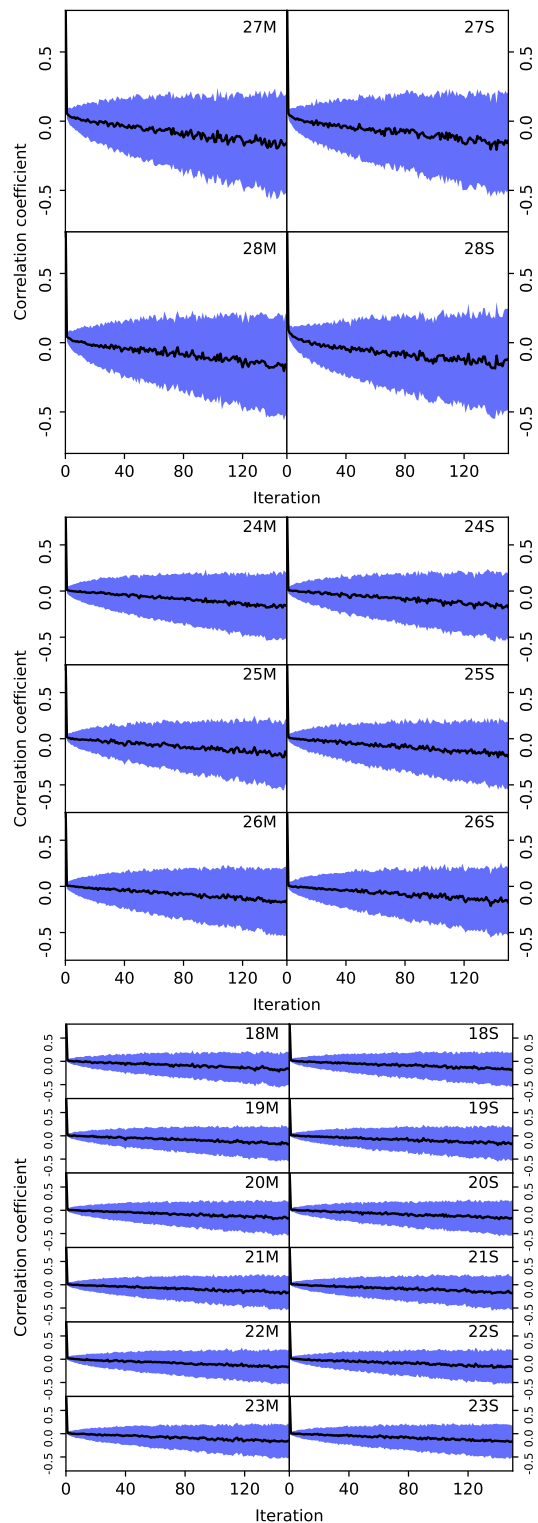


Fig. 9: Correlation coefficients as a function of distance between Gibbs samples for 30 (*top panel*), 44 (*middle panel*), and 70 GHz (*bottom panel*) detectors. The black thick line shows the mean value for all PIDs, while the blue band shows the 1σ error bars.

dominated by the Solar dipole, is retained on the right-hand side. Otherwise, Eq. (17) still represents a Gaussian model, and we should be able to proceed similarly as for g_0 when drawing from the conditional distribution. We do, however, need to ensure that $\sum_i \Delta g_i = 0$, and this will significantly impact the form of the

target distribution. The numerically most convenient method for imposing such a constraint is through the method of Lagrange multipliers.

In general, the method of Lagrange multipliers allows the user to minimize a function $f(\mathbf{x})$ under some set of constraints that may be formulated as $g(\mathbf{x}) = 0$. Without these constraints, one would of course determine x by solving $df/dx = 0$. With additional external constraints, however, it is convenient to instead define the so-called Lagrangian,

$$\mathcal{L}(\mathbf{x}, \lambda) = f(\mathbf{x}) + \lambda g(\mathbf{x}), \quad (18)$$

and set the corresponding partial derivatives with respect to \mathbf{x} and λ equal to zero. It is readily seen that $\partial\mathcal{L}/\partial\lambda = 0$ corresponds directly to $g(\mathbf{x}) = 0$, which is precisely the desired constraint.

Our primary target distribution is

$$\begin{aligned} P(\Delta g | \mathbf{r}, \mathbf{s}^{\text{tot}}, \mathbf{N}) &\propto P(\mathbf{r} | \Delta g, \mathbf{s}^{\text{tot}}, \mathbf{N})P(\Delta g) \\ &\propto \exp\left(\sum_i (\mathbf{r}_i - \Delta g_i \mathbf{s}_i^{\text{tot}})^T \mathbf{N}_i^{-1} (\mathbf{r}_i - \Delta g_i \mathbf{s}_i^{\text{tot}})\right) \end{aligned} \quad (19)$$

where the first line follows from Bayes' theorem, and the second follows from the fact that we assume vanishing covariance between detectors, and that \mathbf{r}_i is Gaussian distributed with a mean of $\Delta g_i \mathbf{s}_i^{\text{tot}}$ and covariance \mathbf{N}_i . We are of course free to minimize the logarithm of this function instead of the function itself, which makes things easier as it takes the exponential away. We may therefore define the following Lagrangian,

$$\mathcal{L}(\Delta g_i, \lambda) = \sum_i (\mathbf{r}_i - \Delta g_i \mathbf{s}_i^{\text{tot}})^T \mathbf{N}_i^{-1} (\mathbf{r}_i - \Delta g_i \mathbf{s}_i^{\text{tot}}) + \lambda \sum_i \Delta g_i, \quad (20)$$

where λ is the Lagrange multiplier.

To optimize this function, we take the derivative with respect to Δg_i and λ to obtain two coupled equations. The first equation takes the form

$$\begin{aligned} \frac{\partial\mathcal{L}}{\partial\Delta g_i} &= 0 \\ \Rightarrow -2(\mathbf{r}_i - \Delta g_i \mathbf{s}_i^{\text{tot}})^T \mathbf{N}_i^{-1} \mathbf{s}_i^{\text{tot}} + \lambda &= 0 \\ \Rightarrow \Delta g_i (\mathbf{s}_i^{\text{tot}})^T \mathbf{N}_i^{-1} \mathbf{s}_i^{\text{tot}} + \frac{1}{2}\lambda &= (\mathbf{r}_i)^T \mathbf{N}_i^{-1} \mathbf{s}_i^{\text{tot}}, \end{aligned} \quad (21)$$

while the second simply reads

$$\begin{aligned} \frac{\partial\mathcal{L}}{\partial\lambda} &= 0 \\ \Rightarrow \sum_i \Delta g_i &= 0. \end{aligned} \quad (22)$$

Jointly solving these linear equations for Δg_i provides estimates with the correct mean. What we require, however, is a sample from the appropriate distribution, and not mean estimates. We must therefore add a fluctuation term, as in Eq. (16). To do so, we note that if it were not for λ , Eq. (21) would have the exact same form as Eq. (16), with \mathbf{s}^{tot} substituted for \mathbf{s}^{orb} . Comparing Eq. (21) with Eq. (16), we then see that the final equation for the desired sample must be

$$\Delta \hat{g}_i (\mathbf{s}_i^{\text{tot}})^T \mathbf{N}_i^{-1} \mathbf{s}_i^{\text{tot}} + \frac{1}{2}\lambda = (\mathbf{r}_i)^T \mathbf{N}_i^{-1} \mathbf{s}_i^{\text{tot}} + \eta \sqrt{(\mathbf{s}_i^{\text{tot}})^T \mathbf{N}_i^{-1} \mathbf{s}_i^{\text{tot}}}, \quad (23)$$

where, as usual, $\eta \sim N(0, 1)$.

Casting this in terms of a linear system with $n_{\text{detector}} + 1$ unknowns, this may be solved straightforwardly with standard numerical libraries. For a two-detector example, the resulting system of equations takes the form

$$\begin{bmatrix} (\mathbf{s}_1^{\text{tot}})^T \mathbf{N}_1^{-1} \mathbf{s}_1^{\text{tot}} & 0 & \frac{1}{2} \\ 0 & (\mathbf{s}_2^{\text{tot}})^T \mathbf{N}_2^{-1} \mathbf{s}_2^{\text{tot}} & \frac{1}{2} \\ 1 & 1 & 0 \end{bmatrix} \begin{bmatrix} \Delta \hat{g}_1 \\ \Delta \hat{g}_2 \\ \lambda \end{bmatrix} = \quad (24)$$

$$\begin{bmatrix} (\mathbf{r}_1)^{\text{tot}} \mathbf{N}_1^{-1} \mathbf{s}_1^{\text{tot}} + \eta_1 \sqrt{(\mathbf{s}_1^{\text{tot}})^T \mathbf{N}_1^{-1} \mathbf{s}_1^{\text{tot}}} \\ (\mathbf{r}_2)^{\text{tot}} \mathbf{N}_2^{-1} \mathbf{s}_2^{\text{tot}} + \eta_2 \sqrt{(\mathbf{s}_2^{\text{tot}})^T \mathbf{N}_2^{-1} \mathbf{s}_2^{\text{tot}}} \\ 0 \end{bmatrix}. \quad (25)$$

3.5. Sampling temporal gain variations with Wiener filter smoothing

Finally, we consider the temporal gain variations, $\delta g_{q,i}$. As before, we write down the following residual,

$$r_{i,t} \equiv d_{i,t} - (g_0 + \Delta g_i) s_{i,t}^{\text{tot}} = \delta g_{q,i} s_{i,t}^{\text{tot}} + n_{i,t}^{\text{tot}}, \quad (26)$$

where we again employ the total signal as a calibrator. The only difference with respect to Eq. (17) is that $\delta g_{q,i}$ now contains multiple elements per detector, and is now a vector in PID space. We can make this point more explicit by writing

$$\mathbf{r}_i \equiv \mathbf{d}_i - (g_0 + \Delta g_i) \mathbf{s}_i^{\text{tot}} = \mathbf{T}_i \delta \mathbf{g}_i + \mathbf{n}_i^{\text{tot}}, \quad (27)$$

where \mathbf{T} is an $n_{\text{samp}} \times n_{\text{scan}}$ -matrix that contains $s_{i,t}^{\text{tot}}$ in element (t, q) for all values of t in scan q . All other elements are zero. Thus, \mathbf{T} projects $\delta \mathbf{g}_i$ into the n_{samp} -dimensional space of \mathbf{r}_i and $\mathbf{n}_i^{\text{tot}}$.

Once again following the procedure in Equation A.3 in [BeyondPlanck \(2022\)](#), we may write down the following sampling equation,

$$\mathbf{T}_i^T \mathbf{N}_i^{-1} \mathbf{T}_i \delta \hat{\mathbf{g}}_i = \mathbf{T}_i^T \mathbf{N}_i^{-1} \mathbf{r}_i + (\mathbf{T}_i^T \mathbf{N}_i^{-1} \mathbf{T}_i)^{\frac{1}{2}} \boldsymbol{\eta}, \quad (28)$$

where $\boldsymbol{\eta} \sim N(\mathbf{0}, \mathbf{I})$ is a random Gaussian vector of length n_{scan} .

In its current form, Eq. (28) assumes that $\delta g_{q,i}$ is uncorrelated between scans. As discussed by [Planck Collaboration VIII \(2014\)](#), [Planck Collaboration VIII \(2016\)](#), [Planck Collaboration III \(2020\)](#), and [Planck Collaboration Int. LVII \(2020\)](#), this is not an efficient model for the *Planck* LFI data, because the gain is primarily determined by the thermal environment of the instrument, which is quite stable in time. It is therefore advantageous, and in practice necessary, to enforce some form of smoothing between $\delta g_{q,i}$ to obtain robust results.

3.5.1. Wiener filtering

The smoothing approach we adopt here is *Wiener filtering*. Although this approach has been applied to other parts of the CMB analysis pipeline such as CMB and noise estimation, it has never before been applied to the gain estimation process. In Bayesian terms, we have so far been drawing samples from the *likelihood function* $\mathcal{L}(\delta \mathbf{g}_i)$, which, since our actual goal is to draw samples from the *posterior* distribution of $\delta \mathbf{g}_i$, means that we are implicitly assuming a uniform prior on this parameter, which in turn means that we let the estimates of $\delta \mathbf{g}_i$ be completely determined by the data alone.

In addition, this means we assume no correlations between the elements in the $\delta \mathbf{g}_i$ vector, as the likelihood function is separable into independent probability distribution functions – an

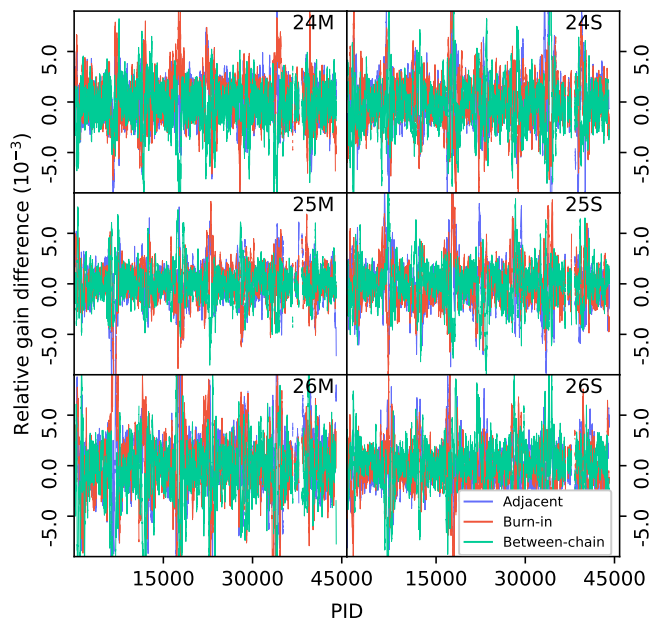


Fig. 10: Relative differences between the last sample in one of the BEYONDPLANCK chains and the sample adjacent to the last sample (blue line), the initial sample (the burn-in difference; red line) and the last sample in another chain (green line), for selected detectors.

effect of this is that Eq. (28) is really a set of independent equations that can be solved sequentially.

Wiener filtering the data essentially amounts to applying a Gaussian prior to the estimation process, meaning that instead of drawing samples from $\mathcal{L}(\delta\mathbf{g}_i)$ alone, we draw samples from $\mathcal{L}(\delta\mathbf{g}_i)P(\delta\mathbf{g}_i)$, where $P(\delta\mathbf{g}_i)$ is the Gaussian prior we want to apply, which in turn will depend on how we *a priori* expect the gain fluctuations to behave. This process will by construction ensure that for scans with high signal-to-noise, the gain estimates will be set mainly by the observed data, whereas in periods of lower signal-to-noise (such as for dipole minima) the estimates will be prior dominated (and thus less fluctuating than without any prior). In addition, this prior explicitly introduces (physically motivated) correlations between the gain fluctuations of different scans which are taken into account during the sampling process rather than being artificially applied after the fact.

In order to sample from the posterior, we need to draw a sample from the product of two Gaussians, $\mathcal{L}(\delta\mathbf{g}_{q,i})$ and $P(\delta\mathbf{g}_{q,i})$:

$$P(\delta\mathbf{g}_i | \mathbf{d}_i) \propto \mathcal{L}(\delta\mathbf{g}_i)P(\delta\mathbf{g}_i). \quad (29)$$

The proper way to sample from such a distribution is given by Eq. (A.10) in BeyondPlanck (2022). In this case, the procedure amounts to replacing Eq. (28) by

$$(\mathbf{G}^{-1} + \mathbf{T}_i^T \mathbf{N}_i^{-1} \mathbf{T}_i) \delta\hat{\mathbf{g}}_i = \mathbf{T}_i^T \mathbf{N}_i^{-1} \mathbf{r}_i + \mathbf{T}_i^T \mathbf{N}_i^{-1/2} \boldsymbol{\eta}_1 + \mathbf{G}^{-1/2} \boldsymbol{\eta}_2, \quad (30)$$

where \mathbf{G} is the covariance matrix of the Gaussian prior on $\delta\mathbf{g}_{q,i}$, and where $\boldsymbol{\eta}_1$ and $\boldsymbol{\eta}_2$ are two independent vectors drawn from a normal distribution with unity variance.

Eq. (30) is, in contrast to Eq. (28), no longer possible to solve scan-by-scan, as the covariance matrix \mathbf{G} introduces cross-scan correlations. To invert this system, we use the conjugate gradient solver procedure described in BeyondPlanck (2022).

Our prior should reflect our knowledge about the gain fluctuations - namely, that such fluctuations are related to fluctuations in the detector electronics. Such fluctuations are generally modelled as having a so-called "pink noise" or $1/f$ spectrum, which means that the gain fluctuation covariance matrix \mathbf{G} can be written as

$$\mathbf{G}(f) = \sigma_0^2 \left(\frac{f}{f_{\text{knee}}} \right)^\alpha. \quad (31)$$

Here, α , f_{knee} and σ_0 are parameters to be determined; for a complete marginalization over these degrees of freedom, they can be made part of the general Gibbs chain in which we are sampling the gains, and an additional sampling step for these parameters can be inserted after sampling the gain fluctuations. This is similar to the process described in Ihle et al. (2022), but we only need to sample a single set of parameters per detector, not one set per scan as in the correlated noise case, since the data points in the gain fluctuation case are the scan themselves, not the individual detector samples.

In the case of LFI processing, we have found that fixing α , σ_0 and f_{knee} instead of sampling over them gives the seemingly best results in terms of gain stability and CMB solutions. For the current paper, through trial, error, and by-eye inspection we've found that fixing the parameters to the following values makes the prior behave as desired: $\alpha = -2.5$, $\sigma_0 = 3 \cdot 10^{-4} \text{ V}^2/\text{K}^2$, $f_{\text{knee}} = 1 \text{ hr}^{-1}$. Although this might seem like an arbitrary choice, the fine-tuning represented here is not substantially different from the fine-tuning of window widths needed for the boxcar smoothing approach used by the Planck DPC.

4. Validation by controlled simulations

As described by Brilenkov et al. (2022), the BEYONDPLANCK analysis framework includes a simulation tool that allows us to input a controlled simulation whose aspects are all perfectly known, and we can use this to validate the reconstructed posterior distributions. The main results from a simulation that considers only one year of LFI 30 GHz observations are presented by Brilenkov et al. (2022). Here, we reproduce some of those results that pertain to the gain estimation results. This simulation includes only CMB (fluctuations, Solar and orbital dipole), correlated and white noise, and gain fluctuations. We then perform an end-to-end Commander analysis in which we sample \mathbf{a}^{CMB} , \mathbf{n}^{corr} , and \mathbf{g} , with no other ancillary data; this is thus a test of the core gain estimation, correlated noise estimation, and mapmaking routines, but not of, say, component separation or sidelobe estimation; those are validated through separate means. The analysis comprises 3,000 samples and the first 1,000 are discarded as burn-in (although these are still included in the trace-plots below).

First, we show in Fig. 5 the total gain samples as a function of Gibbs iteration for one randomly chosen PID for each of the four 30 GHz detectors, and the horizontal line shows the true input. These trace-plots show both that the chains fluctuate around the input gain values, and that their scatter provides a meaningful estimate of the uncertainties. However, we also see that the correlation lengths are significant. This is due to a strong degeneracy between the absolute gain and the CMB Solar dipole when analyzing only a small subset of the data, in this case only one year of 30 GHz observations. When analyzing jointly all data from all channels, the CMB Solar dipole signal-to-noise ratio increases dramatically, and the correlation length goes down, as shown in Sec. 5.

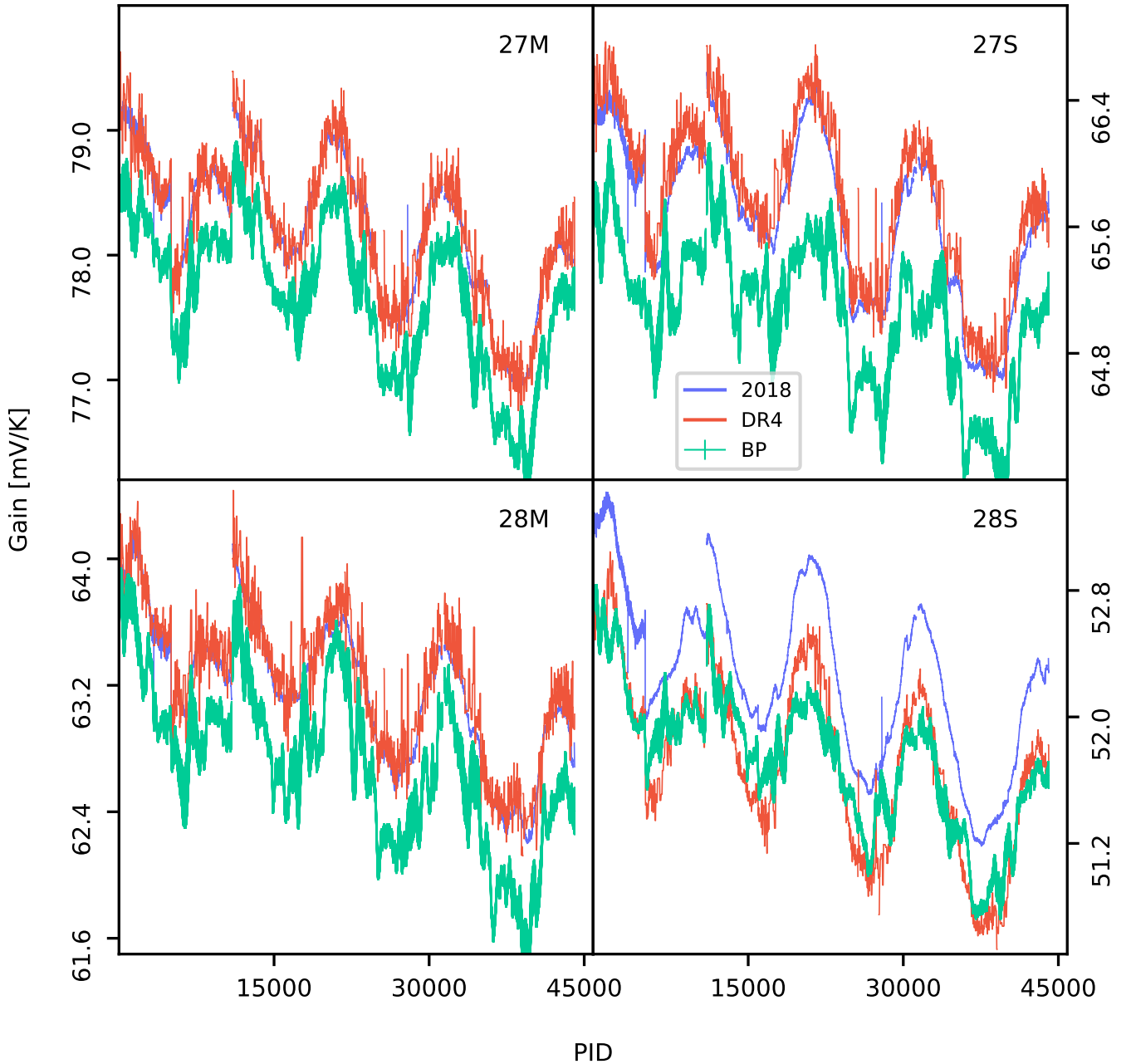


Fig. 11: Comparison of gain estimates for the 30 GHz detectors for *Planck* 2018, *Planck* DR4, and BEYONDPLANCK. The width of the BEYONDPLANCK line is given by the Monte Carlo uncertainty of the chains.

To validate all scans and detectors, Fig. 6 shows the relative reconstruction bias measured in units of standard deviations, i.e.,

$$\epsilon \equiv \frac{g_{q,i}^{\text{in}} - \bar{g}_{q,i}}{\sigma_{q,i}} \quad (32)$$

where $g_{q,i}^{\text{in}}$ is the true input total gain, $\bar{g}_{q,i}$ is the mean sample total gain estimated over all the samples for a given PID and detector, and $\sigma_{q,i}$ is the sample standard deviation. Thus, the figure shows the deviation of the output gain solution from the input in units of standard deviation. Overall, most samples lies within $\pm 2\sigma$, although there are a few notable outliers. It is also worth noting

that the gains are intrinsically correlated in time, and this causes the apparent correlation in this figure.

Finally, in Fig. 7 we show corresponding histograms of the same quantity, but this time aggregated over all PIDs for a given detector. Ideally, these should be Gaussian distributed with zero mean and unit standard deviation. Overall, we see that gain values are generally well-recovered with small biases and reasonable uncertainties. The non-Gaussian features are due to the long correlation lengths seen in Fig. 6, which implies that the number of independent samples in these functions is limited.

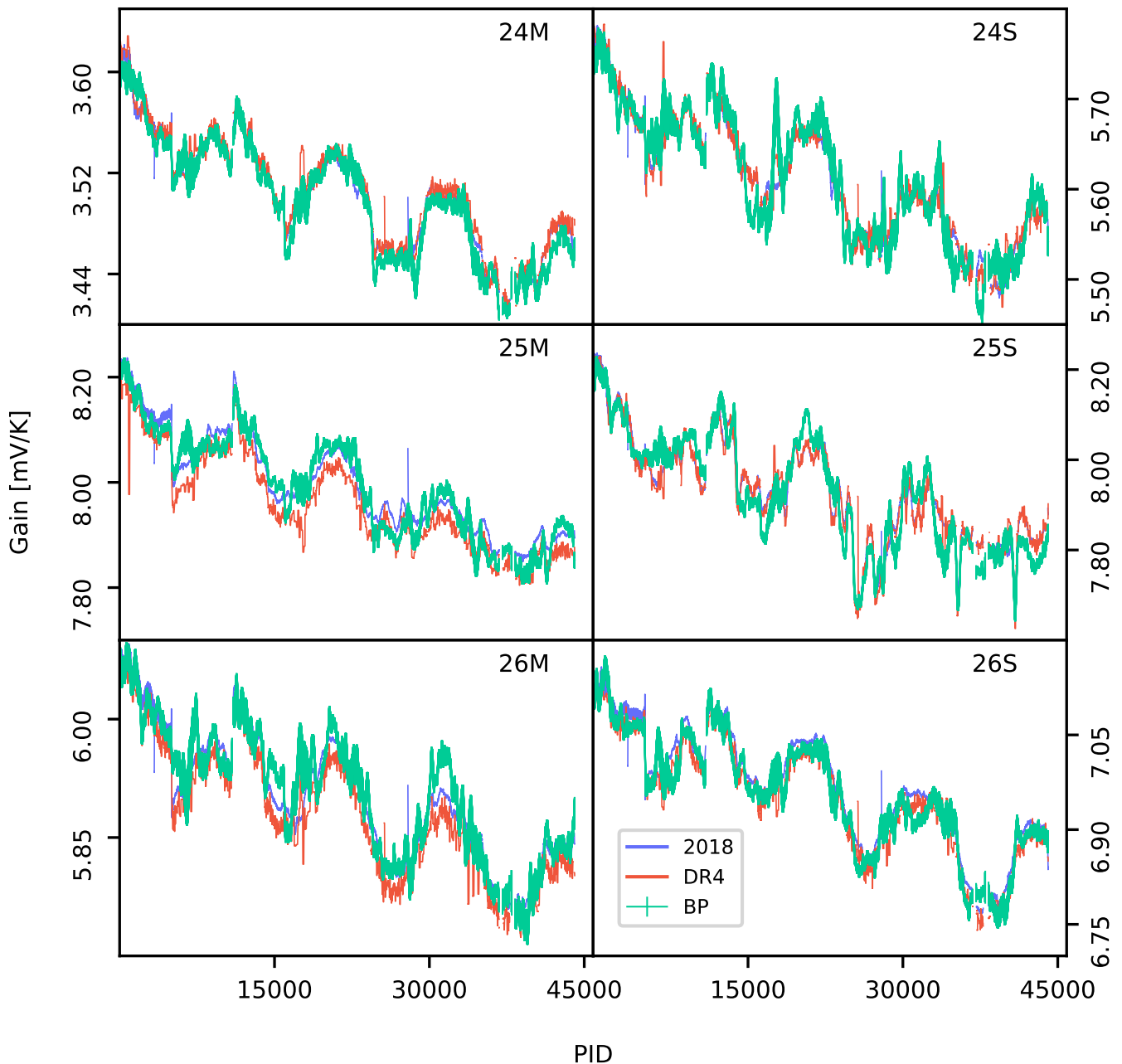


Fig. 12: Comparison of gain estimates for the 44 GHz detectors. See Fig. 11 for details.

5. Results

We are now finally ready to present gain estimates for each *Planck* LFI radiometer, as estimated within the end-to-end Bayesian BEYONDPLANCK analysis framework.

5.1. Gain posterior distributions

We start by considering the sampling efficiency of the Monte Carlo chains produced with the above algorithm in terms of mixing and Markov chain correlation lengths. Figure 8 shows total gain as a function of Gibbs iteration for some representative radiometers and PIDs. We see that overall, the chains are stable and mix well.

A more quantitative confirmation of the good mixing of the chains can be seen in Fig. 9, which shows the correlation lengths across all PIDs (black line is the estimated mean correlation length, whereas the blue bands show the estimated standard deviation). All detectors exhibit correlation coefficients less than 10% after only a few samples.

In Fig. 10, we show relative differences between the last sample of the chain and the first drawn sample (red line), and we compare that to the similar relative difference with the second-to-last sample in the chain (blue line), as well as an in-between chain comparison (green line). We see that even the first sample of the chain is as close to the final solution as the next-to-last sample, and the conditional burn-in period with respect to the gain does not significantly affect our results. Long-term burn-in

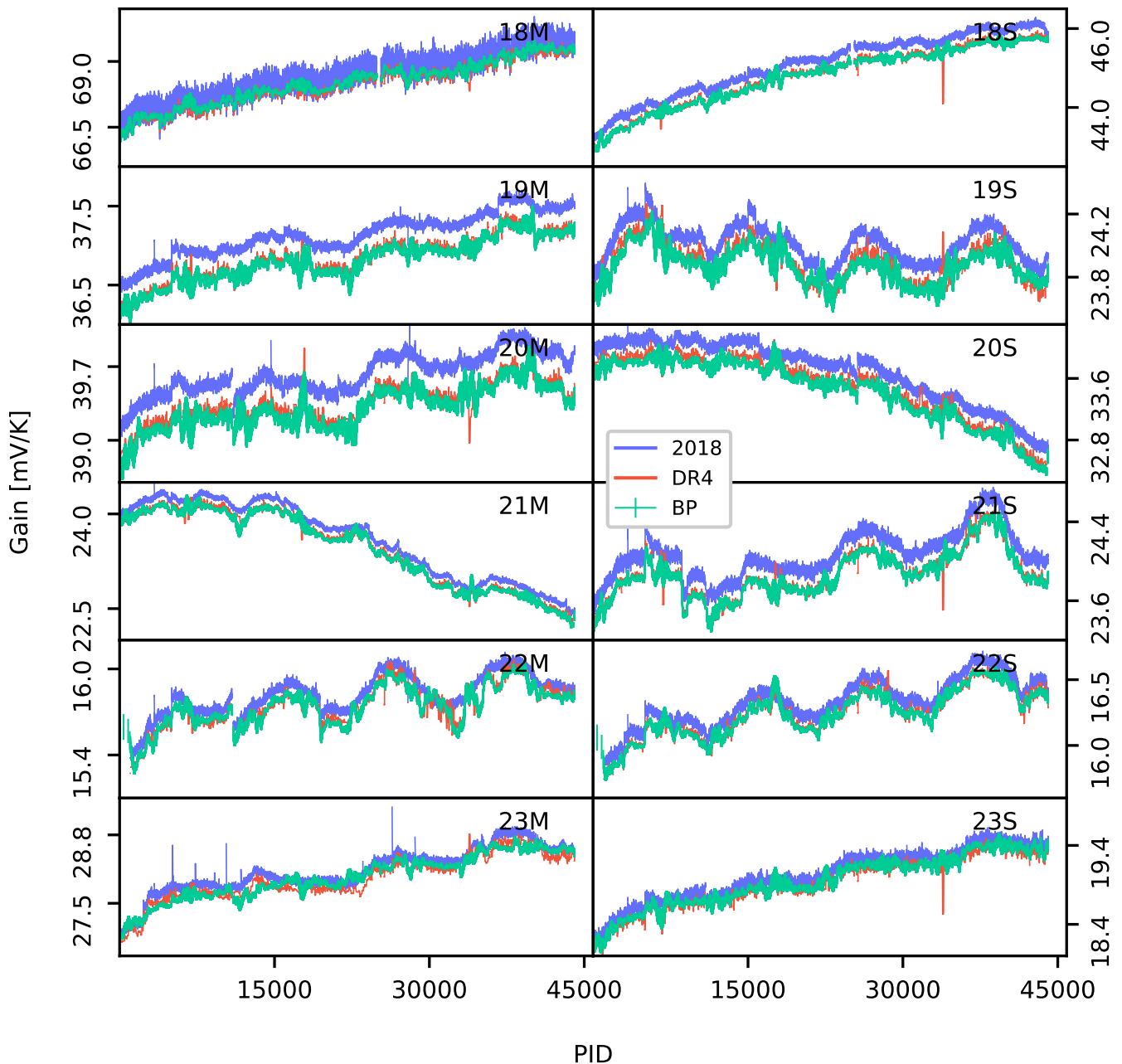


Fig. 13: Comparison of gain estimates for the 70 GHz detectors. See Fig. 11 for details.

is caused indirectly through correlations with other parameters in the system. Because of these external correlations, we follow [BeyondPlanck \(2022\)](#), and omit the first 200 samples when presenting the final gain estimates.

In Figs. 11–13, we compare the gain factors derived by BEYONDPLANCK, *Planck* DR4 and *Planck* 2018 for each detector. For BEYONDPLANCK, the widths of each curve represent 1σ posterior confidence regions as evaluated directly from the Gibbs chains (after omitting 200 samples for burn-in), while for the other two solutions we only show final best-fit estimates.

Overall, the largest differences between BEYONDPLANCK and the other two pipelines are observed in the 30 GHz channel. In particular, we find that the BEYONDPLANCK gain model is systematically lower than the 2018 model by about 0.84 % and than

DR4 by about 0.67 % for this channel, which translates into frequency maps that are about 0.84 % (or 0.67 %) *brighter*. We also see that the DR4 and 2018 models agree very well for three of the radiometers, while 28S is an outlier, for which DR4 is close to BEYONDPLANCK.

The 30 GHz channel is the most difficult to calibrate among all three LFI channels, because of its brighter foreground signal, and the different ways in which the three pipelines handle this fact makes the above-mentioned gain solution differences less surprising: The DR4 process treats this channel separately, in that this channel is analyzed without priors on polarized foregrounds. The resulting map is then subsequently used as a spatial polarization prior for the 44 and 70 GHz channels ([Planck Collaboration Int. LVII 2020](#)). In comparison, the 2018 approach

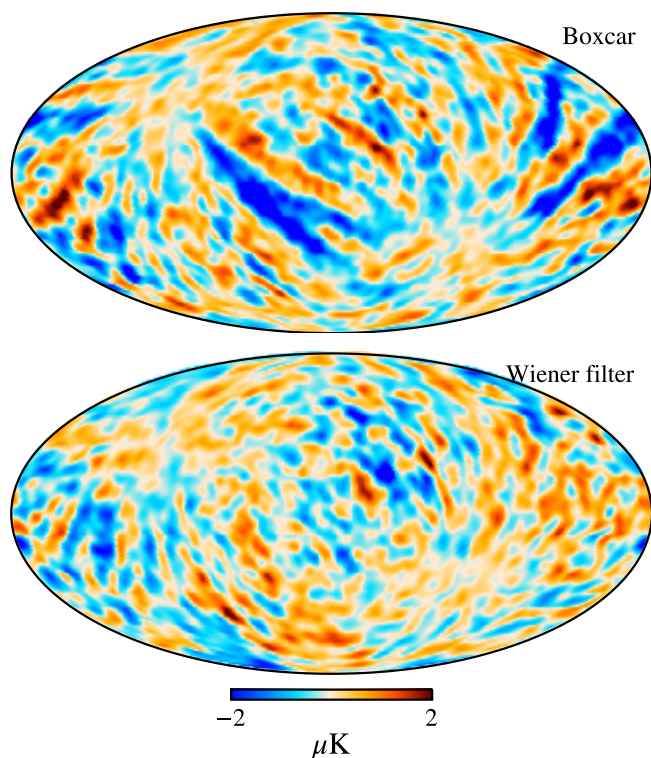


Fig. 14: Map of the correlated noise, n^{corr} , of the Q Stokes parameter for the 44 GHz frequency channel, smoothed to an effective angular resolution of 5° FWHM. The top figure is the map resulting from a boxcar smoothed gain solution, whereas the bottom figure is the map which results from smoothing the gain solution with a Wiener filter.

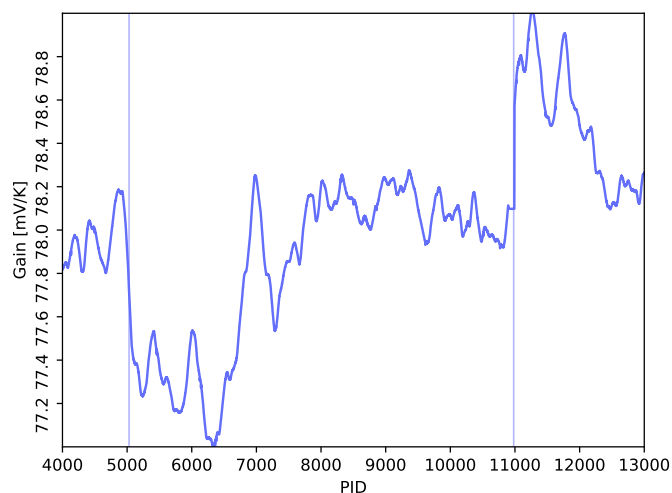


Fig. 15: Examples of jumps seen in the gain factors. The line shows the Wiener filter solution for the 27M detector, while the vertical lines show the locations of the jumps.

also assumes vanishing CMB polarization during calibration, but this approach make no distinction between the orbital and Solar dipole with respect to absolute gain calibration (as both DR4 and BEYONDPANCK do), but rather assumes that the fitted foreground model is sufficiently accurate. In contrast, the BEYONDPANCK pipeline does not treat the 30 GHz channel differently

in any way, and also does not assume that the CMB polarization signal vanishes (except for the single quadrupole mode, as discussed in Sect. 2.4). Instead, it uses *WMAP* information to support the foreground modelling, and to constrain the poorly measured modes in LFI. Overall, these algorithmic differences lead to the observed deviations between the various solutions.

The relative differences are smaller for 44 and 70 GHz: -0.04% (44 GHz) and -0.64% (70 GHz) between BEYONDPANCK and the *Planck* 2018 model, and 0.12% (44 GHz) and -0.03% (70 GHz) between BEYONDPANCK and *Planck* DR4. There is generally good agreement between the three pipelines for these two channels, although *Planck* 2018 is generally a higher absolute calibration than for the two others. Differences between BEYONDPANCK and the two other pipelines are expected due to the joint nature of the BEYONDPANCK approach, and the different ways in which the smoothing of the solutions are performed – BEYONDPANCK uses the Wiener filter smoothing method, *Planck* 2018 uses boxcar averaging, and DR4 does not smooth the solution after estimation at all.

5.2. Effects of different gain smoothing approaches on correlated noise stripes

Since the Wiener filtering approach used in this paper has not previously been used for smoothing gain estimates, we compared it with a more conventional boxcar smoothing approach with similar smoothing windows as used by *Planck* DR4 – that is, smoothing windows that dynamically change with the dipole amplitude so as to make the smoothing length shorter in areas of higher signal-to-noise (i.e. dipole maxima).

When comparing the results of these two approaches, we found that with boxcar averaging, the gain solutions behave more like the original *Planck* 2018 solutions than is the case with Wiener filtering. However, we also found that boxcar smoothing results in correlated noise solutions with strong “stripes” in the binned polarization maps, especially Stokes Q . Reducing the window sizes would mitigate this to some degree (although it introduced other issues, like gain spikes in the low signal-to-noise regime), and we therefore find it likely that the correlated noise stripes are related to an “over-smoothing” of the gain solution.

With the Wiener filter process, we are, modulo the exact form of the prior covariance matrix, smoothing the data in an optimal way – in high signal-to-noise areas, the signal is allowed to determine the solution, and in low signal-to-noise areas, the prior ensures that the solution does not become nonphysical. In Figure 14, we show a comparison of the effect of these two approaches on the Stokes Q map. In this figure, the only difference in the underlying sampling algorithm is the choice of boxcar smoothing and Wiener filtering, and it is reassuring to find that Wiener filtering, in line with expectations, is apparently able to find smooth gain solutions that avoid the problem of over-smoothing.

5.3. Gain jumps

As noted from the beginning of the *Planck* experiment (see, e.g., [Planck Collaboration XXVIII 2014](#)), the physical gain of the instrument exhibits several sharp jumps. These jumps are related to changes in the thermal environment of the instrument – an example of such an event is the turning off of the 20 K sorption cooler. Not all of the events are well understood, and can mainly be traced after an initial gain estimation.

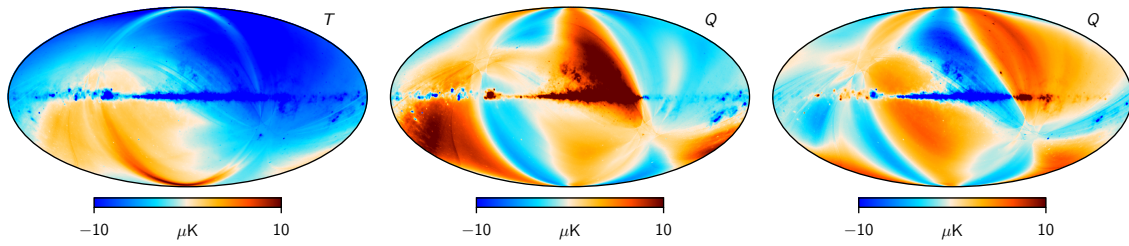


Fig. 16: Gain residual template for the LFI 30 GHz channel, produced in the *Planck* 2018 analysis through manual iteration between calibration, mapmaking and component separation (Planck Collaboration II 2020).

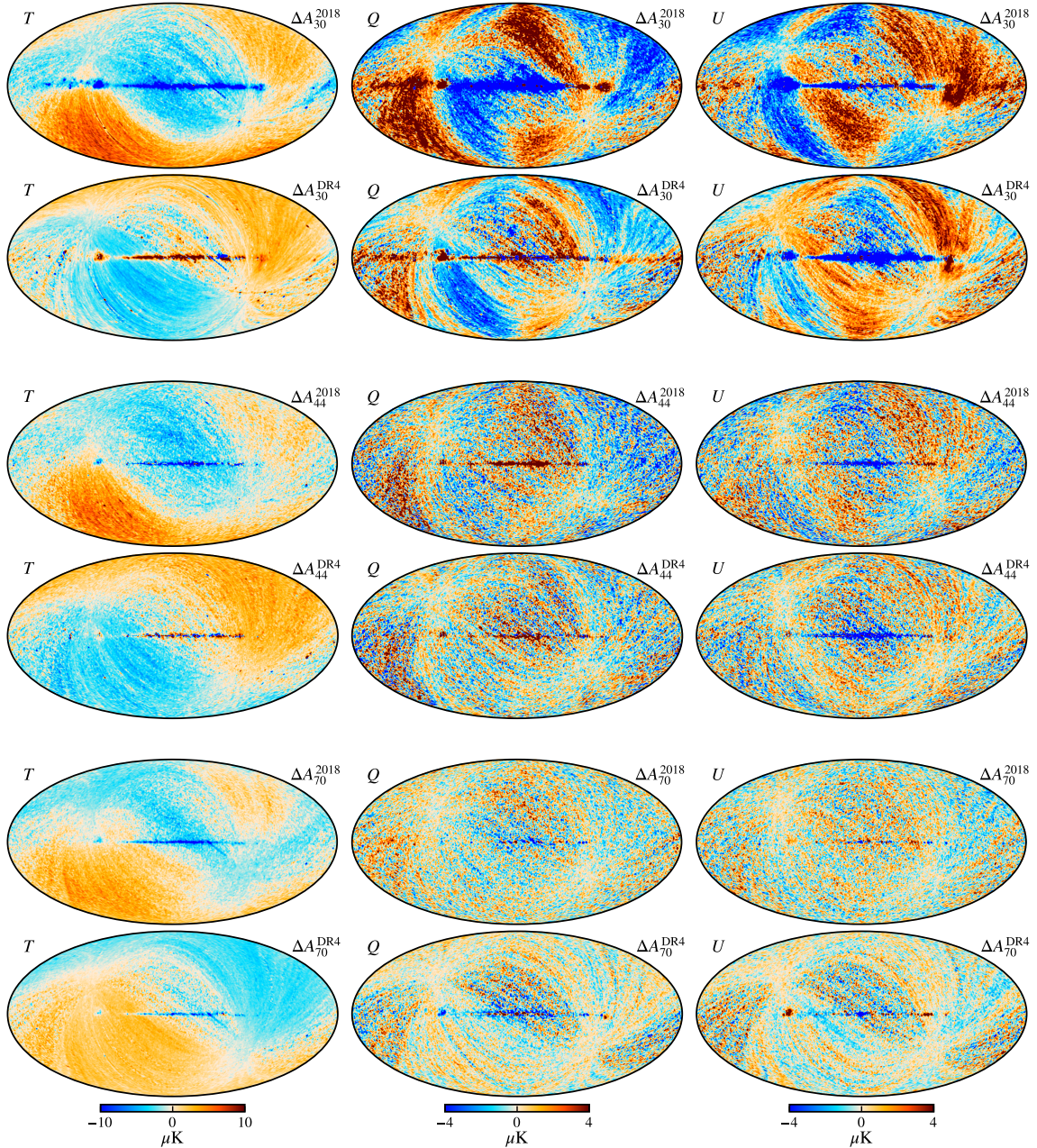


Fig. 17: Differences between BEYONDPLANCK and *Planck* 2018 or *Planck* DR4 frequency maps, smoothed to a common angular resolution of 2° FWHM. Columns show Stokes T , Q , and U parameters, respectively, while rows show pairwise differences with respect to the pipeline indicated in the panel labels. A constant offset has been removed from the temperature maps, while all other modes are retained. The 2018 maps have been scaled by their respective beam normalization prior to subtraction. Reproduced from Suur-Uski et al. (2022).

Such jumps must be accounted for in any gain estimation approach that isn't purely data-driven – i.e. if we are applying priors in any way that set up expected correlated behaviors between the gain factors over the mission. We find that indeed the Wiener filter approach is able to account for such jumps without any extra hard-coding (see Fig. 15, where a Wiener filter solution applied globally to the whole PID range is shown along with two jumps), another advantage of this smoothing method compared to the boxcar approach, where such jumps must be specified in the code and explicitly excluded from the averaging.

5.4. Comparison with external data

To understand the combined impact of the various gain model differences discussed above, it is useful to compare the final BEYONDPLANCK frequency maps with externally processed observations, both from *WMAP* and *Planck*. In this respect, we note that both the *Planck* 2018 and *WMAP* data sets are associated with sets of correction templates that track known systematic effects (or poorly measured modes) in the respective sky maps. For the *Planck* 2018 30 GHz channel, this template is shown in Fig. 16. As discussed by [Planck Collaboration II \(2020\)](#), this template was produced by iterating between calibration and component separation, and therefore traces uncertainties in the gain model due to foreground uncertainties. Furthermore, due to limited time, only four full iterations of this type were completed for the *Planck* 2018 analysis, and one must therefore expect that there are still residuals of this type present in the final sky maps at some level.

With this in mind, we show in Fig. 17 BEYONDPLANCK–DR4 and BEYONDPLANCK–*Planck* 2018 difference maps for Stokes I , Q , and U (columns), for all three LFI frequencies (rows). The first, third and fifth rows show differences with respect to *Planck* 2018, while the second, fourth and sixth rows show differences with respect to DR4. Several features in these difference maps are interesting from the calibration perspective. Starting with the DR4 temperature difference maps, we see that all three channels are dominated by a clean dipole-like residual aligned with the Solar CMB dipole. This shows that the BEYONDPLANCK and DR4 temperature maps are morphologically very similar, but have different absolute calibration. We also see that the temperature map difference between BEYONDPLANCK and DR4 exhibits a flip in the dipole direction going from 30 and 44 to 70 GHz. This sign change is consistent with the differences in the calibration factors between 44 and 70 GHz reported in Table 10 in [Planck Collaboration Int. LVII \(2020\)](#), finding a difference of 0.31 % between the absolute calibration of the 44 and 70 GHz channels. Since the CMB Solar dipole has an amplitude of about $3360 \mu\text{K}$, this relative difference translates into an absolute temperature difference of roughly $10 \mu\text{K}$ in the observed sky signal, which is fully consistent with the dipole differences we see in Fig. 17. In comparison, the *Planck* 2018 vs BP difference maps in temperature (line 1, 3, and 5) show a more prominent quadrupolar structure with a morphology that might resemble the effect of bandpass mismatch leakage ([Planck Collaboration X 2016](#); [Planck Collaboration Int. LVII 2020](#)).

For polarization, the most striking differences are seen in the 30 GHz channel, for which variations at the $4 \mu\text{K}$ level are seen over large fractions of the sky. Furthermore, these residuals correlated very closely with the *Planck* 2018 gain template shown in Fig. 16, suggesting that they are indeed caused by foreground-induced gain residuals. The same patterns are also seen in the DR4 difference maps, but with a notably lower level.

For the 44 GHz maps, we note that the Stokes Q difference maps show correlated noise stripes similar to those highlighted in the top figure in Fig. 14. However, we also note that these structures have different amplitudes in *Planck* DR4 and *Planck* 2018, and these stripes are therefore present in at least one of the other pipelines as well, and possibly both.

Figure 18 shows a similar comparison between the various *Planck* 30 GHz maps and the *WMAP* K -band channel ([Bennett et al. 2013](#)). In this case, all maps have been smoothed to a common angular resolution of 3° FWHM, and the K -band map has been scaled by a factor of 0.495 to account for the different center frequencies of the two maps while adopting a synchrotron-like spectral index of $\beta_s = -3.1$. From top to bottom, the first three rows show difference maps with respect to *Planck* 2018, *Planck* DR4, and BEYONDPLANCK.

Overall, we see a clear progression in agreement with respect to *WMAP* K -band, in the sense that BEYONDPLANCK shows smaller residuals than *Planck* DR4, which in turn shows smaller residuals than *Planck* 2018. Furthermore, we note that the strong residuals traced by the LFI gain template in Fig. 16 are most pronounced in the *Planck* 2018 map.

At the same time, we also observe significant coherent large-scale features in the difference map between BEYONDPLANCK and K -band. To at least partially understand these, we show the *WMAP* transmission imbalance templates derived by [Jarosik et al. \(2007\)](#) in the bottom row of Fig. 17. These templates trace poorly measured modes due to the differential nature of the *WMAP* instrument. Although corrections for this effect are applied to the final K -band sky maps, the uncertainty on the template amplitudes is estimated to 20 %. Considering the tight correlation between the BEYONDPLANCK–*WMAP* difference map and the transmission imbalance template, it seems clear that at least a significant fraction of the remaining residual may be explained in terms of this effect. Of course, this also suggests that a future joint analysis between *Planck* and *WMAP* in time-domain will be able to constrain the *WMAP* transmission imbalance parameters to much higher precision, and *Planck* data can thereby be used to break an important internal degeneracy in *WMAP*. As reported by [Watts et al. \(2022\)](#), this work has already started, but a full exploration of time-ordered *WMAP* data is outside the scope of the current analysis. We also emphasize that the current BEYONDPLANCK analysis only uses low-resolution *WMAP* polarization data for which a full covariance matrix is available, and these modes are appropriately down-weighted in those matrices.

6. Conclusions

We have presented the BEYONDPLANCK approach to gain calibration within the larger Commander Gibbs sampling framework. This framework relies directly on the Solar and orbital dipoles for relative and absolute calibration, respectively, and accounts for astrophysical foreground and instrumental systematics through global modelling.

One critically important difference with respect to previous *Planck* LFI analysis efforts is the fact that we actively use external data to break internal *Planck* degeneracies, and in particular *WMAP* observations. This significantly alleviates the need for imposing strong algorithmic priors during the calibration process. Most notably, while both the *Planck* 2018 and *Planck* DR4 pipelines assumed CMB polarization to be negligible on all angular scales during the calibration phase, we only assume that the CMB quadrupole is negligible. The reason we still make this assumption is that the *Planck* scanning strategy renders the CMB quadrupole very nearly perfectly degenerate with the CMB Solar

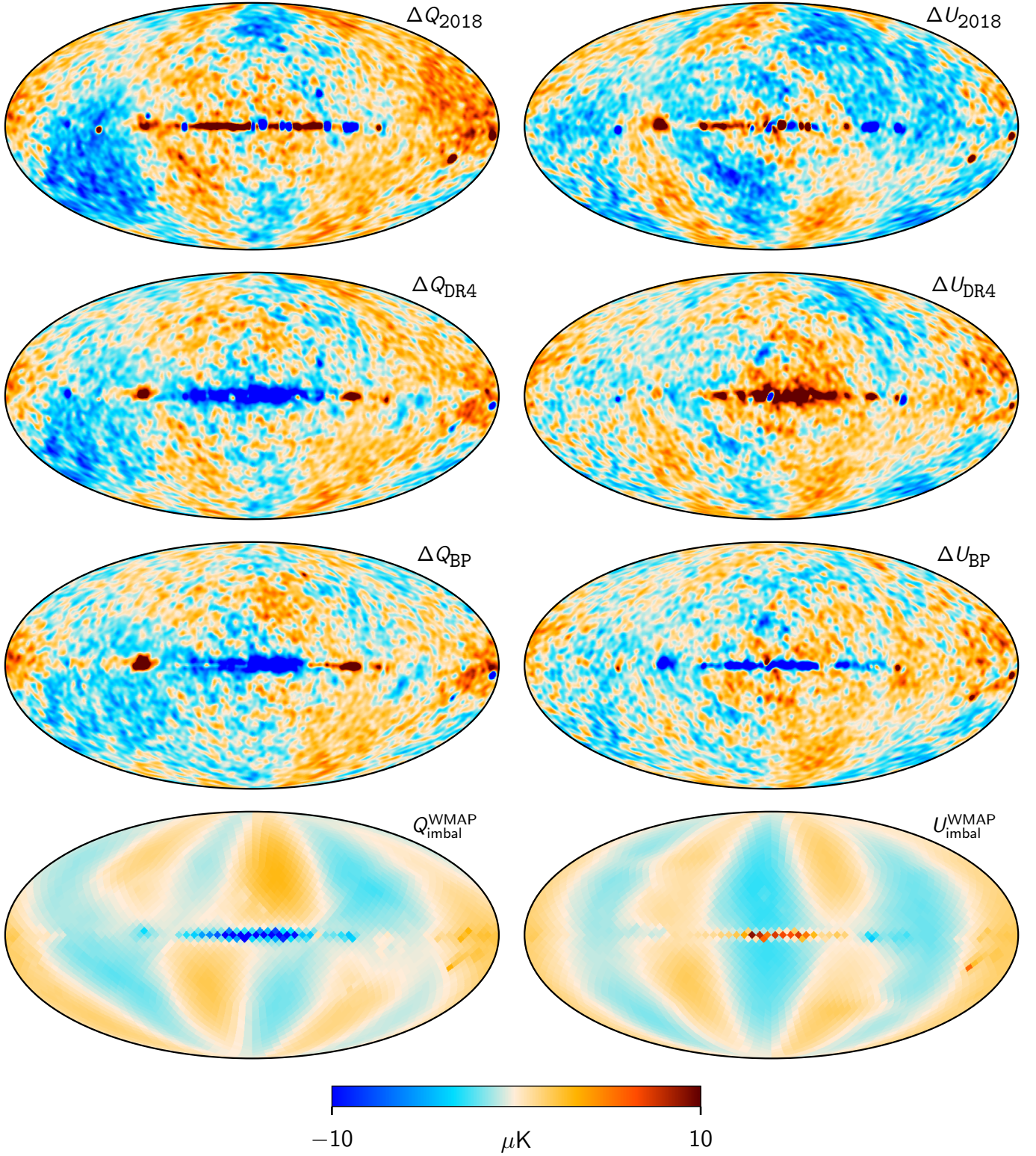


Fig. 18: Difference maps between the *Planck* 30 GHz and *WMAP* *K*-band maps for *Planck* 2018 (first row), *Planck* DR4 (second row), and BEYONDPLANCK (third row). All maps have been smoothed to a common angular resolution of 3° FWHM before evaluating the differences. The *WMAP* *K*-band map has been scaled by a factor of 0.495 to account for different center frequencies, assuming a synchrotron spectral index of $\beta_s = -3.1$. The bottom row shows one of the *WMAP* *K*-band transmission imbalance templates discussed by Jarosik et al. (2007), which accounts for known poorly measured modes in the *WMAP* data.

dipole coupled to subtle gain fluctuations; a hypothetical future and well-designed satellite mission should not require this prior, as long as its scanning strategy modulates the CMB dipole on sufficiently short time-scales and with good cross-linking.

Overall, we find good agreement between the BEYONDPLANCK and previous gain models. The biggest differences are observed in the LFI 30 GHz channel, with gain variations of 0.84 % between *Planck* 2018 and BEYONDPLANCK. These differences result in subtle but significant temperature and polarization residuals. When comparing these with external *WMAP* *K*-band observations, it seems clear that the BEYONDPLANCK LFI maps are generally cleaner than previous renditions with respect to gain residuals. At the same time, we emphasize that these differences are also consistent with previously published error estimates, as presented by the *Planck* 2018 and *Planck* DR4 teams themselves. For instance, the morphology of the *Planck* 2018 polarization residuals matches previously published LFI DPC gain residual templates ([Planck Collaboration II 2020](#)), and the DR4 absolute calibration differences are fully consistent with internal DR4 estimates ([Planck Collaboration Int. LVII 2020](#)). These results are thus neither novel nor surprising, but they simply highlight the inherent advantages of global analysis, using complementary data sets to break internal degeneracies.

Finally, we note that even though the procedures outlined in this paper have been aimed at modelling the LFI detectors, there is nothing about the data model or methodology that is unique for LFI. The method should be directly applicable for other data sets and experiments as well, and, indeed, a preliminary *WMAP* analysis is already underway ([Watts et al. 2022](#)).

Acknowledgements. We thank Prof. Pedro Ferreira for useful suggestions, comments and discussions, and Dr. Diana Mjaschkova-Pascual for administrative support. We also thank the entire *Planck* and *WMAP* teams for invaluable support and discussions, and for their dedicated efforts through several decades without which this work would not be possible. The current work has received funding from the European Union’s Horizon 2020 research and innovation programme under grant agreement numbers 776282 (COMPET-4; BEYONDPLANCK), 772253 (ERC; BRIS2COSMOLOGY), and 819478 (ERC; COSMOGLOBE). In addition, the collaboration acknowledges support from ESA; ASI and INAF (Italy); NASA and DoE (USA); Tekes, Academy of Finland (grant no. 295113), CSC, and Magnus Ehrnrooth foundation (Finland); RCN (Norway; grant nos. 263011, 274990); and PRACE (EU).

References

- Bennett, C. L., Larson, D., Weiland, J. L., et al. 2013, *ApJS*, 208, 20
 BeyondPlanck. 2022, A&A, in preparation [[arXiv:2011.05609](#)]
 Brilenkov et al. 2022, A&A, in preparation [[arXiv:201x.xxxxx](#)]
 de Bernardis, P., Ade, P. A. R., Bock, J. J., et al. 2000, *Nature*, 404, 955
 Delouis, J. M., Pagano, L., Mottet, S., Puget, J. L., & Vibert, L. 2019, A&A, 629, A38
 Fixsen, D. J. 2009, *ApJ*, 707, 916
 Godard, B., Croon, M., Budnik, F., & Morley, T. 2009, in Proceedings of the 21st International Symposium on Space Flight Dynamics (ISSFD), Toulouse
 Greason, M. R., Limon, M., Wollack, E., et al. 2012, *Nine-Year Explanatory Supplement*, 5th edn., Greenbelt, MD: NASA/GSFC
 Hinshaw, G., Weiland, J. L., Hill, R. S., et al. 2009, *The Astrophysical Journal Supplement Series*, 180, 225–245
 Ihle et al. 2022, A&A, in preparation [[arXiv:2011.06650](#)]
 Jarosik, N., Barnes, C., Greason, M. R., et al. 2007, *ApJS*, 170, 263
 Kogut, A., Fixsen, D. J., Chuss, D. T., et al. 2011, *J. Cosmology Astropart. Phys.*, 2011, 025
 Kovac, J. M., Leitch, E. M., Pryke, C., et al. 2002, *Nature*, 420, 772
 Planck Collaboration I. 2011, A&A, 536, A1
 Planck Collaboration II. 2014, A&A, 571, A2
 Planck Collaboration VIII. 2014, A&A, 571, A8
 Planck Collaboration XXVIII. 2014, A&A, 571, A28
 Planck Collaboration II. 2016, A&A, 594, A2
 Planck Collaboration V. 2016, A&A, 594, A5
 Planck Collaboration VIII. 2016, A&A, 594, A8
 Planck Collaboration X. 2016, A&A, 594, A10

- Planck Collaboration I. 2020, A&A, 641, A1
 Planck Collaboration II. 2020, A&A, 641, A2
 Planck Collaboration III. 2020, A&A, 641, A3
 Planck Collaboration IV. 2018, A&A, 641, A4
 Planck Collaboration Int. XLVI. 2016, A&A, 596, A107
 Planck Collaboration Int. LVII. 2020, A&A, 643, A42
 Smoot, G. F., Bennett, C. L., Kogut, A., et al. 1992, *ApJ*, 396, L1
 Suur-Uski et al. 2022, A&A, in preparation [[arXiv:201x.xxxxx](#)]
 Watts et al. 2022, A&A, in preparation [[arXiv:2202.11979](#)]